Journal of Neuroinflammation

RESEARCH

Open Access

TREM2 affects DAM-like cell transformation in the acute phase of TBI in mice by regulating microglial glycolysis

Lin Wang[1,2†], Diqing Ouyang[1†], Lin Li[1], Yunchuan Cao[1], Yingwen Wang[1], Nina Gu[1], Zhaosi Zhang[1], Zhao Li[3], Shuang Tang[4], Hui Tang[2], Yuan Zhang[2*], Xiaochuan Sun[1*] and Jin Yan[1*]

Abstract

Background Traumatic brain injury (TBI) is characterized by high mortality and disability rates. Disease-associated microglia (DAM) are a newly discovered subtype of microglia. However, their presence and function in the acute phase of TBI remain unclear. Although glycolysis is important for microglial differentiation, its regulatory role in DAM transformation during the acute phase of TBI is still unclear. In this study, we investigated the functions of DAM-like cells in the acute phase of TBI in mice, as well as the relationship between their transformation and glycolysis.

Methods In this study, a controlled cortical impact model was used to induce TBI in adult male wild-type (WT) C57BL/6 mice and adult male TREM2 knockout mice. Various techniques were used to assess the role of DAM-like cells in TBI and the effects of glycolysis on DAM-like cells, including RT–qPCR, immunofluorescence assays, behavioural tests, extracellular acidification rate (ECAR) tests, Western blot analysis, cell magnetic sorting and culture, glucose and lactate assays, and flow cytometry.

Results DAM-like cells were observed in the acute phase of TBI in mice, and their transformation depended on TREM2 expression. TREM2 knockout impaired neurological recovery in TBI mice, possibly due in part to their role in clearing debris and secreting VEGFa and BDNF. Moreover, DAM-like cells exhibited significantly increased glycolytic activity. TREM2 regulated the AKT–mTOR–HIF-1α pathway and glycolysis in microglia in the acute phase of TBI. The increase in glycolysis in microglia partially contributed to the transformation of DAM-like cells in the acute phase of TBI in mice.

Conclusions Taken together, the results of our study demonstrated that DAM-like cells were present in the acute phase of TBI in mice. TREM2 might influence DAM-like cell transformation by modulating the glycolysis of microglia. Our results provide a new possible pathway for intervening TBI.

†Lin Wang and Diqing Ouyang contributed equally to this work.

*Correspondence:
Yuan Zhang
1013791298@qq.com
Xiaochuan Sun
sunxiaochuan@cqmu.edu.cn
Jin Yan
yanjin@hospital.cqmu.edu.cn

Full list of author information is available at the end of the article

Keywords Traumatic brain injury, Microglia, Disease-associated microglia, Glycolysis, Triggering receptor expressed on myeloid cells 2

Introduction

Traumatic brain injury (TBI) is a prominent global health concern, causing long-term neurological impairments in millions of individuals annually [1]. Immediately after TBI, cells at the site of injury undergo activation and proliferation. In addition to the influx of circulating white blood cells into the damaged area, brain tissue-resident microglia swiftly respond to injury. Throughout the phases of brain injury, repair, and regeneration, microglia play dual roles, being beneficial or detrimental depending on the state of microglia [2]. This versatility stems from their remarkable plasticity, enabling them to adopt distinct molecular phenotypes and functional profiles in response to varying environmental cues, thereby eliciting diverse effects [3]. With the rapid development of single-cell genomics technology, many previously unknown cellular subsets, including a novel cluster of microglia termed disease-associated microglia (DAM), have been identified in the context of ageing and Alzheimer's disease (AD) [4]. DAMs are intricately linked to neurodegenerative pathologies, and their differentiation is dependent on TREM2 expression [5]. Emerging evidence underscores the neuroprotective capacity of this microglial subtype in neurodegenerative diseases [6]. Nevertheless, current studies have focused predominantly on chronic conditions, and less is known about the roles of DAM in acute injuries, particularly in TBI, with the underlying mechanisms warranting further elucidation.

Although DAM signatures have been detected in several chronic neurological diseases, including AD, multiple sclerosis (MS), and amyotrophic lateral sclerosis (ALS) [5, 7, 8], DAM signatures have also been detected in some acute neurological conditions. Additionally, a unique type of microglia with enhanced antioxidant function and markers are similar to those of DAM, designated stroke-associated microglia (SAM), has been identified in acute ischaemic stroke mice, showing potent antioxidant properties that mitigate ROS-induced damage to protect brain tissue following acute brain injury [9]. DAM also appears to play an influential role in acute neurological infections. The DAM phenotype has been observed in mice infected with *Staphylococcus aureus* and *Toxoplasma gondii* [10]. Nevertheless, their precise functions in acute infection have not been thoroughly explored. In a mouse model of traumatic spinal cord injury, a previously uncharacterized subtype of microglia with striking similarities to DAM was identified. Additionally, DAM-like cells have been detected in human spinal cord injury specimens. Further investigation suggested that DAM may contribute to an improved prognosis in acute spinal cord injury [11]. Interestingly, DAM-like cells have been detected in the brain tissues of mice during the chronic phase (> 30 days) after traumatic brain injury (TBI), suggesting a possible exacerbation of neuronal damage [12]. Moreover, DAM have also been recently identified in mice in the acute phase of TBI by single-cell RNA sequencing [13]. Nevertheless, the precise functions of DAM at acute time points (≤ 7 days) after injury are currently lacking, and the molecular mechanisms underlying DAM transformation require further investigation.

In recent years, research regarding the close relationship between immune cell functions and their metabolic states has given rise to the field of immunometabolism. The functions of immune cells can vary during an immune response, thereby creating the need to adapt their metabolism of glucose, amino acids, lipids, and ketone bodies to support changing cellular activities [14, 15]. The amount of substrate utilized and the type of metabolic pathway activated depend on the phenotype of microglia [16]. Although glycolysis is less efficient at producing ATP than oxidative phosphorylation (OXPHOS), the rate of ATP generation is 10–100 times faster than that of OXPHOS, which is essential for supporting energy-intensive processes such as proliferation, migration, cytokine release, and phagocytosis [17]. Glycolysis in microglia may contribute to providing intermediate metabolites for maintaining cell proliferation, cytokine production, and inflammatory protein synthesis [18]. Moreover, their intermediate metabolites can serve as biosynthetic precursors for regulating inflammatory state transitions and can act as signalling molecules that participate in reshaping the phenotype of immune cells [19]. The transition from OXPHOS to glycolysis can rapidly provide the ATP that microglia require for their activation and phagocytic functions [20]. DAM also appear to undergo a similar shift, as evidenced by the significant upregulation of the HK2 gene, a key player in glycolysis, within DAM-like cells [21]. However, research on the metabolic state of DAM-like cells is lacking, and more in-depth studies are needed.

Triggering receptor expressed on myeloid cells 2 (TREM2) has been found to activate phagocytosis and suppress inflammatory responses to protect neuronal function in experimental ischaemic stroke and intracerebral haemorrhage animal models [22]. TREM2 induces DAP12 phosphorylation, which subsequently recruits and activates spleen tyrosine kinase (SYK), leading to downstream signal activation that ultimately promotes cell proliferation, survival, and phagocytosis, as well as the secretion of cytokines and chemokines [23]. In

our previous study, we reported an increase in TREM2 expression in the acute phase of TBI in mice [24]. Compelling evidence suggests that TREM2 in mice and humans is a crucial regulator of microglial activation and the transition from a homeostatic state to a DAM phenotype [7, 25]. Moreover, microglia with various variants of TREM2, such as the R47H risk variant, exhibit notable metabolic defects, including an inability to convert their metabolism to glycolysis during an immune response [26]. The absence of TREM2 can also lead to alterations in mTOR signalling and decreased ATP levels [27]. Since mTOR is considered a master metabolic regulator, the mechanistic transcriptional control of glycolysis may also be dependent on mTOR [28]. Thus, we hypothesize that the influence of TREM2 on glycolysis and mTOR may also impact the transformation of DAM-like cells.

Therefore, this study aimed to investigate the physiological roles of DAM-like cells, the regulatory mechanisms of microglia differentiation to DAM in TBI model mice, and potential intervention strategies both in vitro and in vivo.

Materials and methods

Animal experiments

To exclude the effect of estrogens on TBI, only male mice were used for this study [29]. C57BL/6 male mice (8–12 weeks old, 20–30 g) were procured from the Animal Centre of Chongqing Medical University (Chongqing, China). Adult male TREM2 knockout mice (C57BL/6J-Trem2em2^{Adiuj}/J, 8–12 weeks old, 22–30 g) were obtained from the Shanghai Model Organisms Centre (Cat# NM-KO-190402, SMOC). The genotyping protocol and results for the TREM2 knockout mice are detailed in Additional file 1: Additional methods and Fig. S1. All the mice were housed in a specific pathogen-free facility with meticulously controlled temperature and humidity, adhering to a 12-hour light–dark cycle with lights on at 6:00. Standard laboratory chow was provided ad libitum to the mice. Random allocation was employed for group assignment, with the experimental group undergoing controlled cortical impact surgery to induce TBI and the control group receiving Sham surgery. Brain tissue samples were harvested from each group on days 1, 2, 3, 7, 21 and 30 post-TBI according to the specific experimental arrangement. The animal experimental procedures were approved by the Animal Care Committee of the Animal Research Centre at Chongqing Medical University in accordance with the guidelines outlined by the National Institutes of Health for laboratory animal care and use. The detailed experimental design and animal allocation information are shown in supplemental materials.

TBI model

TBI was induced by a controlled cortical impact surgery [24]. Briefly, the mice were anaesthetized via an intraperitoneal injection of pentobarbital sodium (0.05 mg/g). A midline incision was made, the skin was retracted, and a 4 mm diameter craniotomy was performed 2 mm to the right of the midline, above the right parietal cortex between the lambda and bregma sutures. The skull cap was carefully removed without damaging the underlying meninges. A TBI model was established via the TBI-0310 TBI model system (Precision Systems and Instrumentation, Fairfax, VA, USA) with a 2.5 mm diameter impact tip vertically over the exposed cortical surface. The parameters for the TBI were set as follows: impact velocity, 5.0 m/s; deformation depth, 1.0 mm; and duration, 200 milliseconds. Post surgery, the incision was sutured, and the mice were placed on a warming pad to maintain a core body temperature of 37 ± 0.5 °C until they recovered from anaesthesia.

Immunofluorescence staining

The mice were euthanized under deep anaesthesia, perfused with 4 °C PBS to flush out red blood cells from the vasculature, and subsequently fixed with 4% paraformaldehyde (PFA). The collected brains were kept overnight in 4% PFA at 4 °C, followed by sequential incubation in 20% and 30% sucrose overnight at 4 °C. The brains were then embedded in optimal cutting temperature compound and sectioned into 20 μm-thick coronal slices. After being washed with PBS, the sections were blocked with PBS + 5% BSA and permeabilized with 0.5% Triton-X 100 in blocking solution. Primary antibodies were added at the indicated dilutions overnight.

The primary antibodies used included goat polyclonal anti-IBA1 (1:200, Cat# ab5076, Abcam), mouse monoclonal anti-TIMP2 (1:100, Cat# ab1828, Abcam), rabbit monoclonal anti-PKM2 (1:100, Cat# 4053T, CST), rabbit monoclonal anti-M-CSF (1:100, Cat# ab233387, Abcam), rabbit polyclonal anti-VEGFa (1:100, Cat# ab39250, Abcam), rabbit polyclonal anti-NeuN (1:100, Cat# ab104225, Abcam), and mouse monoclonal anti-BDNF (1:100, Cat# ab205067, Abcam). After thorough washing with PBS three times for 10 min each, the sections were incubated with secondary antibodies (1:400; Beyotime Institute of Biotechnology) conjugated to Alexa-Fluor405/488/594 for 1 h at room temperature. The cell nuclei were counterstained with 4',6-diamidino-2-phenylindole (DAPI; Sigma–Aldrich).

For each sample, three to four corresponding sections were collected every 300 μm, with 6 mice per group for analysis. Three random 20× or 40× images encompassing the lesion core per section were analyzed. The measured values represent the mean of all the section measurements per mouse. Sections depicting all lesion sites were

collected, and the regions of interest (ROIs) for the captured images were demarcated by white boxes in the Figures, then digitally magnified 10 times. Imaging was conducted using a Leica DM4 B fluorescence microscope (Leica, DM4 B, Wetzlar, Hesse, Germany) with a 10×eyepiece and a 10, 20 or 40×objective, utilizing identical exposure settings for quantitative analysis in each experimental run. Using ImageJ for quantification, the number of $IBA1^+$ cells co-expressing other target proteins was quantified. For the analysis of three-color fluorescence staining, DAM-like cells were first manually identified and counted, followed by measurement of the mean grey intensity of the target proteins expressed in these DAM-like cells. Immunofluorescence colocalization was analysed via the Coloc 2 plugin in ImageJ software (ImageJ 1.4, NIH, Bethesda, MD, USA). The quantification of immunopositive cells was performed using ImageJ software (ImageJ 1.4, NIH, Bethesda, MD, USA) and is presented as the average cell count per high-power field in single-staining experiments or as the percentage of main marker cells to co-marker cells per HPF in double-staining experiments. All counts were conducted in a blinded manner.

Western blot analysis

Brain tissue samples, encompassing the injury site (approximately 5 mm * 5 mm * 3 mm), were harvested for total protein extraction using RIPA lysis buffer supplemented with protease and phosphatase inhibitors. The supernatant was collected, and the total protein concentration was determined. Equal amounts of protein (20 μg) from each sample were added to 4× Laemmli sample buffer and subjected to sodium dodecyl sulfate–polyacrylamide gel electrophoresis (SDS–PAGE) (Invitrogen), followed by transfer onto a polyvinylidene fluoride (PVDF) membrane (Millipore, Boston, MA, USA). The membrane was washed with TBST buffer (Tris-buffered saline containing 0.1% Tween 20), blocked with 5% nonfat milk for 1 h at room temperature, and subsequently incubated overnight at 4 °C with primary antibodies, including rabbit polyclonal anti-p-Akt 473 (1:1000, Cat# 28731-1-AP, Proteintech), rabbit polyclonal anti-Akt (1:1000, Cat# 10176-2-AP, Proteintech), rabbit monoclonal anti-β-Actin (1:5000, Cat# ab213262, Abcam), mouse monoclonal anti-mTOR (1:1000, Cat# 66888-1-Ig, Proteintech), mouse monoclonal anti-p-mTOR (Ser2448) (1:1000, Cat# 67778-1-Ig, Proteintech), and rabbit polyclonal anti-Hif-1α (1:1000, Cat# 20960-1-AP, Proteintech) antibodies. Following primary antibody incubation, the membrane was subjected to additional washes, incubated with an HRP-conjugated secondary antibody at room temperature for 1 h, and then subjected to further washing before visualization via enhanced chemiluminescence using the Bio-Rad ChemiDoc MP imaging system. Immunoblot quantification was conducted via ImageJ (ImageJ 1.4, NIH, Bethesda, MD, USA). The raw Western blot bands are shown in supplementary materials (Fig. S4).

Isolation of microglia and DAM-like cells

Adult model mice were deeply anaesthetized with pentobarbital sodium and disinfected with alcohol. Immediately after removal, the injured ipsilateral brain hemispheres, excluding the cerebellum, were dissected and washed with prechilled PBS. The brain tissues were mechanically and enzymatically dissociated using an adult brain dissociation kit (Cat# 130-107-677; Miltenyi Biotec) according to the manufacturer's instructions. After debris and myelin were removed with cell debris removal buffers and erythrocytes with red blood cell removal buffers, the cell pellets were resuspended in D-PBS containing 0.5% BSA, and specific cell types were isolated. In brief, microglia were separated via MicroBeads coated with an anti-CD11b antibody (Cat# 130-093-634; Miltenyi Biotec), whereas DAM-like cells were isolated via MicroBeads coated with an anti-CD11c antibody (Cat# 130-125-835; Miltenyi Biotec), and then used CD11b magnetic beads to isolate out no-DAM microglia from the remaining cells. The isolated live microglia were immediately used in various cellular experiments. For RNA extraction, isolated cells were flash-frozen in liquid nitrogen and stored at -80 °C until use. For cell culture, the sorted cells were promptly cultured in Dulbecco's modified Eagle's medium (DMEM) (Cat# 103575; Agilent) containing 1% Antibiotic-Antimycotic (Cat#15240062; Thermo Fisher Scientific) and 2 mM GlutaMAX (Cat# 35050061; Gibco), 10% fetal bovine serum (Cat# SH30070; Hyclone), and mCSF1 (50 ng/ml; Cat# 315-02, Peprotech). For RNA extraction and RT–qPCR analysis, each group has 6 samples, and each sample was pooled from 3 mice brains. For cell culture, each group has 6 samples, and each sample was pooled from 5 mice brains. For flow cytometry analysis, each group has 3 samples, and each sample was pooled from only one mouse brain.

Metabolic analysis

Metabolic analysis was conducted using a Seahorse Extracellular Flux Analyser (XF24) (Seahorse Bioscience, North Billerica, MA, USA) to perform real-time analysis of cellular metabolism. Purified microglia (5×10^4 cells/well) (100 μL/well) isolated from mouse brains were seeded onto a Seahorse-specific cell culture microplate and cultured in a cell culture incubator to allow cell adhesion overnight. Seahorse XF Calibrant solution (1 ml; SeaHorse BioScience, North Billerica, MA, USA) was added to each well of the Seahorse XFe24 Flux Assay Kit plate and incubated at 37 °C in a non-CO_2 cell culture

incubator for 1 h. Prior to measurement, the cells were washed twice with the appropriate assay medium (1 ml) according to the manufacturer's instructions, and the assay medium was added to a final volume of 500 µL/well. The plate was then incubated in a non-CO_2 incubator (37 °C, 1 h). The prepared drugs were gently added to the drug reservoir in the probe plate, and after calibration, the extracellular acidification rate (ECAR) was measured every 8 min for a total of 96 min. During this period, 10 mM glucose, 0.5 µM oligomycin, and 100 mM 2-deoxyglucose (2-DG) were sequentially injected every 24 min. At the end of the experiment, the number of cells in each well was re-counted by cell counter (Rayward C100, Shenzhen, China). The data were normalized to the number of cells, and Seahorse XF24 software automatically calculated the ECAR, with each sample measured in triplicate.

RT–qPCR

Total RNA was extracted from the sorted cells using a total RNA extraction kit (Cat# BSC63S1, Bioer). cDNA synthesis was subsequently conducted with a high-capacity cDNA reverse transcription kit (Cat# HY-K0511A, MCE). Quantitative PCR (qPCR) was performed using SYBR Green real-time PCR master mix (Cat# AG11701, AG) and a LightCycler 96 detection system (Roche). The housekeeping gene β-actin was utilized, and gene expression was determined via the ΔΔCt method. Genes with Ct values exceeding 35 cycles were deemed undetectable, and RNA samples exhibiting low quality or purity were excluded from subsequent analyses. For the qPCR analysis of the cDNA library, custom primers from Shanghai Sangon Biotech were used:

Timp2 forward sequence: CGCTTAGCATCACCCA GAAGAAGAG, Timp2 reverse sequence: AGTCCATC CAGAGGCACTCATCC; M-Csf forward sequence: A GGATGAGGACAGACAGGTGGAAC, M-Csf reverse sequence: GGTAGGAGAGGGTAGTGGTGGATG; Cd9 forward sequence: CCAGTCGTTCGTGCCTCTTGTC, Cd9 reverse sequence: GCCAGCGAGCCAGAAGATG AAG; Lpl forward sequence: CGCTCTCAGATGCCCT ACAAAGTG, Lpl reverse sequence: TTGTGTTGCTT GCCATCCTCAGTC; Cst7 forward sequence: GGCAC GCAGAGAGTCCTTT GATG, Cst7 reverse sequence: C TTCCCACACTACCACCTTGTTGAC; GLUT1 forward sequence: CTCACCACGCTTTGGTCTCT, GLUT1 reverse sequence: CCCAGTTTGGAGAAG CCCAT; GLUT2 forward sequence: ATCACCGGAACCTTGGC TTT, GLUT2 reverse sequence: CAGCTTTCCGGTCA TCCAGT; GLUT3 forward sequence: CCTACCAAGTG AGGGACTG C, GLUT3 reverse sequence: GGCCCAG GATCAGCATTTCA; GLUT4 forward sequence: TTGG CTCCCTTCAGTTTGGC, GLUT4 reverse sequence: CGTAGTGAGGGTGCCTTGTG; GLUT5 forward sequence: TGCCTTTGGCTCATCCTTCC, GLUT5 reverse sequence: TAAAGCCCCCAAAGGGGAAC. The quality of the PCR products was assessed via electrophoresis in a 1.5% agarose gel. Raw CT data were normalized to the mean of β-actin via the 2^{-ddCt} method.

Pharmacological interventions

2-DG intervention

2-DG was administered via intraperitoneal injection at a dosage of 400 mg/kg/d, with an equivalent volume of PBS injected for the control group [30]. The administration of 2-DG started one week prior to the initiation of TBI modelling and was continued for 72 h following successful modelling. The 2-DG administration was conducted in the evening, and the administration times were kept consistent across all treatments.

FBP intervention

FBP was administered via intraperitoneal injection at a dosage of 500 mg/kg/d [31], and an equivalent volume of PBS was administered to the control group. The administration of FBP started one week prior to the initiation of TBI modelling. Following successful modelling, FBP administration was continued for 72 h. Cell was treated with FBP at a concentration of 10 mM [32].

2-NBDG injection

The mice were maintained for 72 h post-TBI, with a 16-hour fasting period preceding tail vein injection of 2-NBDG at a dose of 375 µg per mouse (storage solution concentration: 2.5 mg/mL; injection volume: 150 µL per mouse) [33]. One-hour postinjection, the mice were anaesthetized, and perfusion was conducted according to the immunofluorescence requirements. After complete retrieval of the brain tissue, subsequent fixation, dehydration, and sectioning were performed for further immunostaining.

COG1410 injection

Lactated Ringer's solution containing 0.2 mg/mL COG1410 was injected via the tail vein at 1 h and 24 h post-TBI at a dose of 5 µL/g, resulting in a final COG1410 dose of 1 mg/kg [24].

Fluorescent glucose uptake assay

Sorted microglia from all experimental groups were seeded into 96-well plates precoated with polylysine at a density of 5×10^4 per well, with 5 replicates per group. After seeding, the cells were gently shaken and allowed to settle for 1 h in a laminar flow hood until the cells settled evenly. The cell culture plates were then transferred to a cell culture incubator for 2 h to allow the cells to adhere to the walls, achieving a cell density of 80–90% after adhesion. The culture medium was removed, and

the wells were washed twice with PBS. Subsequently, 150 μL of 50 μmol/L 2-NBDG solution was added, and the plates were incubated at 37 °C and 5% CO2 for 30 min in a cell culture incubator. Afterwards, the 2-NBDG solution was removed, and the wells were washed three times with PBS. The plates were observed under a fluorescence microscope to capture fluorescence images. The fluorescence intensity was quantitatively analysed via ImageJ software.

Behaviour experiments

Neurological severity score (NSS) evaluation

The NSS evaluates general behaviour, alertness, balance, and motor abilities through 10 distinct tasks [34]. The NSS scoring was performed on mice in each group before surgery and on days 1, 2, and 3 post surgery. Each failure results in one point. A score of 0 represents minimal deficits, whereas a score of 10 indicates severe deficits. To minimize the scorer's subjective awareness bias, the assessment should be blinded to the specific group assignments of the experimental animals.

Wire grip test

As previously reported [35], a 45 cm long, 3 mm diameter metal wire is suspended between two vertical sticks 45 cm above the ground. Prior to the experiment, mice were trained to grasp a metal wire with their forepaws and maintain their body weight for at least 60 s, which was considered a successful trial. If the animal fell before the end of the training, it was immediately returned to the wire and required to re-establish its grip. During testing, the mice were placed in the middle of the wire and observed for 60s to record and assess their latency to fall. Each mouse was measured three times, followed by a re-measurement after a 5–10-minute interval. The average value was calculated.

Rotarod test

The accelerated rotarod was used to assess motor coordination [36]. For this, mice were trained for 3–5 days on rotarod rotating at 4 RPM so that animals may walk forward to keep balance. Training is considered complete when mice can stay on the rod rotating at 4 RPM for at least 1 min. On the test day, mice were placed on the rod rotating at 4 RPM and then rotation was set in acceleration mode (accelerated by 3 rpm every 10 s until it reaches 30 rpm). The latency of mice to fall of the rod was recorded and evaluated. During testing, three measurements were recorded, with each measurement followed by a re-test after a 5–10-minute interval. The average of these measurements was then calculated.

Beam walking test

In the beam walking test [35], the mice are placed on a wooden beam (12 mm diameter, 1 m long, 50 cm high) and allowed to longitudinally traverse a black box located on the other side of the beam driven by their inherent phototaxis. The number of left foot slips and the time taken to cross the entire beam are recorded. A foot slip is defined as slipping of the left paw off the beam surface. The mice are placed at one end of the beam and trained to cross the balance beam to reach the escape box at the other end. If they stop midway to sniff or look around, researchers should gently encourage them to continue moving forward by lightly poking or pushing them from behind with a gloved finger. Once the mice reach the safety box, they are allowed to remain there for 15 s. There is a 10-minute break between the two training sessions. The mice underwent a 3-day training period before surgery, and their performance was assessed at 13-day post-TBI. All experimenters and animal caretakers were blind to the experimental groups. Each mouse was measured three times with a 5-minute interval, and the average value was taken. The data were analyzed by the first experimenter and verified by the second experimenter using video recordings.

Morris water maze (MWM)

In the MWM experiment [37], the mice were allowed to habituate to the testing apparatus (diameter 110 cm) and were screened for visual impairments one day prior to experimentation. The maze was filled with turbid water, which was refreshed daily and maintained at a temperature range of 19–22 °C. Artificial demarcations divided the maze into four quadrants, with a platform (diameter of 10 cm) fixed 1 cm below the water surface at one centre of a randomly selected quadrant. Distinctive objects, varying in colour and shape, were affixed to the walls of each quadrant as spatial cues. During training sessions for 5 consecutive days, the mice were allowed 60 s of unrestricted swimming to locate the platform. The mice that failed to locate the platform were gently guided to the platform and allowed to remain for 30 s. Each mouse underwent two training sessions daily, with data representing the average of both trials. Twenty-four hours after the final training session, the platform was removed, and the mice underwent probe trials to evaluate memory retention. Overhead video cameras were used to monitor the swimming activity of each mouse, and the data were automatically recorded via ANY-maze behavioural tracking software (Stoelting).

Open field test (OFT)

Following MWM, the mice were subjected to an open field test [24]. The open field apparatus consisted of an uncovered square box constructed from opaque white

organic acrylic material with dimensions of 50 cm × 50 cm × 40 cm (length × width × height). The box was specifically designed to be nontranslucent and nonreflective, with its floor automatically divided into 25 small squares by software. Positioned directly above the box was a digital camera capable of recording the movement trajectories of the mice, with its field of view encompassing the entire open field. The middle 9 squares of the open field were designated the central zone, while the remaining areas were considered the peripheral zone. The experimental conditions ensured a quiet environment, with soft lighting to minimize glare. Prior to each trial, the open field was meticulously cleaned of any urine or faeces using tissue paper and alcohol. The mice were introduced to the testing room one hour before the experiment was conducted to acclimate to the experimental environment.

The mice were gently placed in the central zone of the open field, and their activity and trajectories were recorded for 5 min. Subsequently, sophisticated software analysis was employed to assess parameters, including the time spent in the central zone versus the periphery, for comprehensive statistical analysis.

Lesion size analysis

21 days post-TBI surgery, mice were perfused with PBS followed by 4% paraformaldehyde, and their brains were harvested. Using a mouse brain sectioning mold, the brain was sliced to a thickness of 1 mm. Brain slices were imaged with a camera, and analysis was performed using ImageJ software (ImageJ 1.4, NIH, Bethesda, MD, USA). As previously described [38], the total lesion volume was determined using the formula: [volume = ΣA × t × ISF], where A = sum of the corrected lesion areas, t = slice thickness (1000 μm), and ISF = inverse of the sampling fraction.

Brain water content assay

On day 3 post-TBI surgery, mice were deeply anesthetized with an intraperitoneal injection of 1% pentobarbital sodium, followed by decapitation. The brain was promptly removed, and the cerebellum and brainstem were discarded. The brain tissue was then separated along the longitudinal cerebral fissure, the healthy hemisphere discarded, and the wet weight of the affected hemisphere was measured. The tissue from the affected hemisphere was placed in a 90 °C oven to dehydrate for 3 days, after which the dry weight was determined. The brain water content was calculated using the following formula: Brain water content (%) = (wet weight-dry weight) / wet weight×100%.

Evans blue tests

On day 3 post-TBI surgery, mice were intravenously injected with Evans blue dye (dissolved in saline at 2% concentration, 2 ml/kg) via the tail vein. 1 h later, when the dye fully circulated within the blood, the mice were then deeply anesthetized with an intraperitoneal injection of 1% pentobarbital sodium. 20 ml of saline and 20 ml of 4% paraformaldehyde were infused into the left ventricle via a catheter. The brain was carefully harvested and weighed. The tissue was subsequently transferred into a centrifuge tube containing 1 ml of PBS, homogenized using a tissue homogenizer, and centrifuged at 15,000 rpm for 5 min at 4 °C. The supernatant (300 μl) was mixed with 700 μl of acetone and incubated at room temperature for 24 h. Then centrifuged at 15,000 rpm for 5 min at 4 °C, the absorbance at 620 nm was measured using a microplate reader as previously described [39]. Evans blue content was quantified by comparing the absorbance to a standard curve created from known concentrations of Evans blue dye.

Glucose and lactate detection

After 24 h of culture in a CO_2-free incubator, the culture media of isolated microglia and DAM-like cells were collected. Lactate levels in the various media were evaluated using a lactate assay kit (Cat#A019-2-1; Nanjing Jiancheng) following the manufacturer's instructions. Additionally, glucose consumption in different groups was determined using a glucose assay kit (Cat# F006-1-1; Nanjing Jiancheng) in accordance with the protocol provided by the manufacturer.

Flow cytometry

The CD11b-MicroBeads sorted microglial cells were subjected to surface staining. Following incubation at room temperature in an Fc block (1:50, Cat# BD 553142, BD Biosciences) for 10 min, the cells were stained with antibodies for at least 15 min at 4 °C in the dark. The antibodies used against mouse antigens included anti-CD45 FITC (1:200, Cat#130-116-500, Miltenyi), anti-CD11b APC (1:200, Cat#130-113-802, Miltenyi), and anti-CD11c FITC (1:200, Cat#117306, Biolegend) antibodies. Flow cytometric (BD Influx, New Jersey, USA) analysis was subsequently performed. Flow cytometry data were analysed using FlowJo v10.7.1.

Statistical analysis

Prior to conducting the analysis, the Shapiro–Wilk test was employed to assess the normality of the variables. When two groups were compared, an unpaired two-tailed Student's t test was employed to determine the significance of differences. For comparisons involving three or more groups, one-way analysis of variance (ANOVA) with Tukey's multiple comparison test or two-way

ANOVA with Sidak's multiple comparison test was used to calculate significant differences. Most of the statistical data in this section are presented as the mean ± standard deviation (SD), unless otherwise specified in the figure legends. All the statistical graphs were generated via GraphPad Prism 9.15, and all the data were derived from at least three independent samples. In this study, the significance levels for all the statistical tests were set at $p \leq 0.05$.

Results

DAM-like cells were identified in the acute phase of TBI in mice

Typical DAM-like cells express genes such as Cst7, Lpl, Cd9, Timp2, and M-Csf [5], and these hallmark DAM genes have been studied and validated in mouse models of ischaemic stroke [9], spinal cord injury [11], and AD [40]. A pooling strategy was implemented to increase the reliability and comparability of the results across specific time points, effectively reducing the impact of random variability. This involved combining injured hemisphere from 3 to 5 mice at each time point into a single sample [11]. We then used CD11b magnetic beads to sort and collect microglial cell suspensions for RT–qPCR analysis (Fig. 1A). Analysis of $CD45^+$ $CD11b^+$ expression by Flow cytometry indicated a microglial cell purity exceeding 95% (Fig. S2). Then, we focused on changes in the expression of hallmark DAM genes in microglia at different phases of TBI, including days 1, 2, 3, 7, 21, and 30 postinjury (Fig. S3 and Fig. 1B-F). Our findings revealed significant upregulation of DAM marker gene expression commencing 3 days post-injury (dpi). To further validate the qPCR results, we conducted immunofluorescence staining to confirm the presence of the DAM hallmark proteins M-CSF and TIMP2 during the acute phase of TBI.

The immunostaining results confirmed the increased of $M\text{-}CSF^+$ (Fig. 1G, H) or $TIMP2^+$ (Fig. 1I, J) microglia in cortical brain sections from the mice at 3 dpi, revealing a notable increase in M-CSF or TIMP2 expression in the microglia surrounding the cortical injury site, with minimal expression observed in the microglia in the brain tissues from the Sham. Furthermore, morphological analysis of microglia showed a significant shortening of the maximum branch and a significant increase in cell soma area after TBI, indicating activation of microglia around the injury site after TBI (Fig. 1K, L).

TREM2 was required for the transformation of DAM-like cells in the acute phase of TBI in mice

Studies have revealed that in chronic neurodegenerative diseases such as AD, there is a notable increase in TREM2 expression within the DAM subset. TREM2 expression is crucial for the transition to the DAM phenotype, and TREM2 gene knockout obstructs DAM transformation [5]. To investigate whether TREM2 plays a similar role in DAM-like cells in TBI, we further examined the impact of TREM2 knockout on DAM-like cell transformation in TBI model mice. First, we assessed the expression of DAM marker genes in microglia isolated from $TREM2^{-/-}$ mice 3 dpi via magnetic bead isolation. Our RT–qPCR experiments revealed that TREM2 expression was essential for expression of DAM marker genes. Compared with WT 3 dpi mice, $TREM2^{-/-}$ 3 dpi mice presented significantly lower expression of DAM marker genes in microglia. Moreover, there was no significant upregulation in the expression of DAM marker genes in microglia between the $TREM2^{-/-}$ Sham group and the $TREM2^{-/-}$ TBI group (Fig. 2A-E). Considering that mRNA expression does not always directly reflect protein expression, we subsequently validated our qPCR results by examining the expression of DAM marker proteins in $TREM2^{-/-}$ TBI model mice. While TIMP2 and M-CSF were expressed in the microglia of WT mice at 3 dpi (Fig. 1G, I), microglia in TREM2 knockout mice of both Sham and TBI groups presented negative immunofluorescence staining results for TIMP2 and M-CSF at 3 dpi (Fig. 2F-I). Therefore, the function of TREM2 in microglia was indispensable for the transformation of DAM-like cells in our TBI model mice.

TREM2 knockout impaired neurological recovery in TBI model mice

Given that TREM2 was required for full acquisition of the DAM signature during the acute phase of TBI in mice. Next, we explored the impact of TREM2 on neurological recovery after TBI. On day 3 post-TBI, compared with WT TBI mice, $TREM2^{-/-}$ TBI mice presented significantly greater NSS score, with markedly lower wire grip scores and rotarod latency (Fig. 3A-C). Then, we performed neuropathological tests on mice that underwent early behavioural testing after TBI, including blood-brain barrier injury by Evans blue assay, brain edema, and neuronal apoptosis. Our results showed that compared to the Sham groups, the TBI groups had more severe BBB damage (Fig. 3D, E), brain edema (Fig. 3F), and neuronal apoptosis (Fig. 3G, H). Furthermore, compared to WT TBI mice, TREM2 knockout TBI mice showed more severe neuropathological outcomes (Fig. 3D-H).

Next, another four cohorts of mice were used to explore chronic neurological function after TBI. On days 13 post-TBI, we performed the beam walking test to evaluate motor function recovery. We found no significant difference in the latency to traverse the beam between WT TBI and $TREM2^{-/-}$ TBI model mice (Fig. 3I). However, $TREM2^{-/-}$ TBI model mice presented an increased number of foot slips (Fig. 3J). To evaluate the impact of TREM2 KO on the recovery of learning and memory

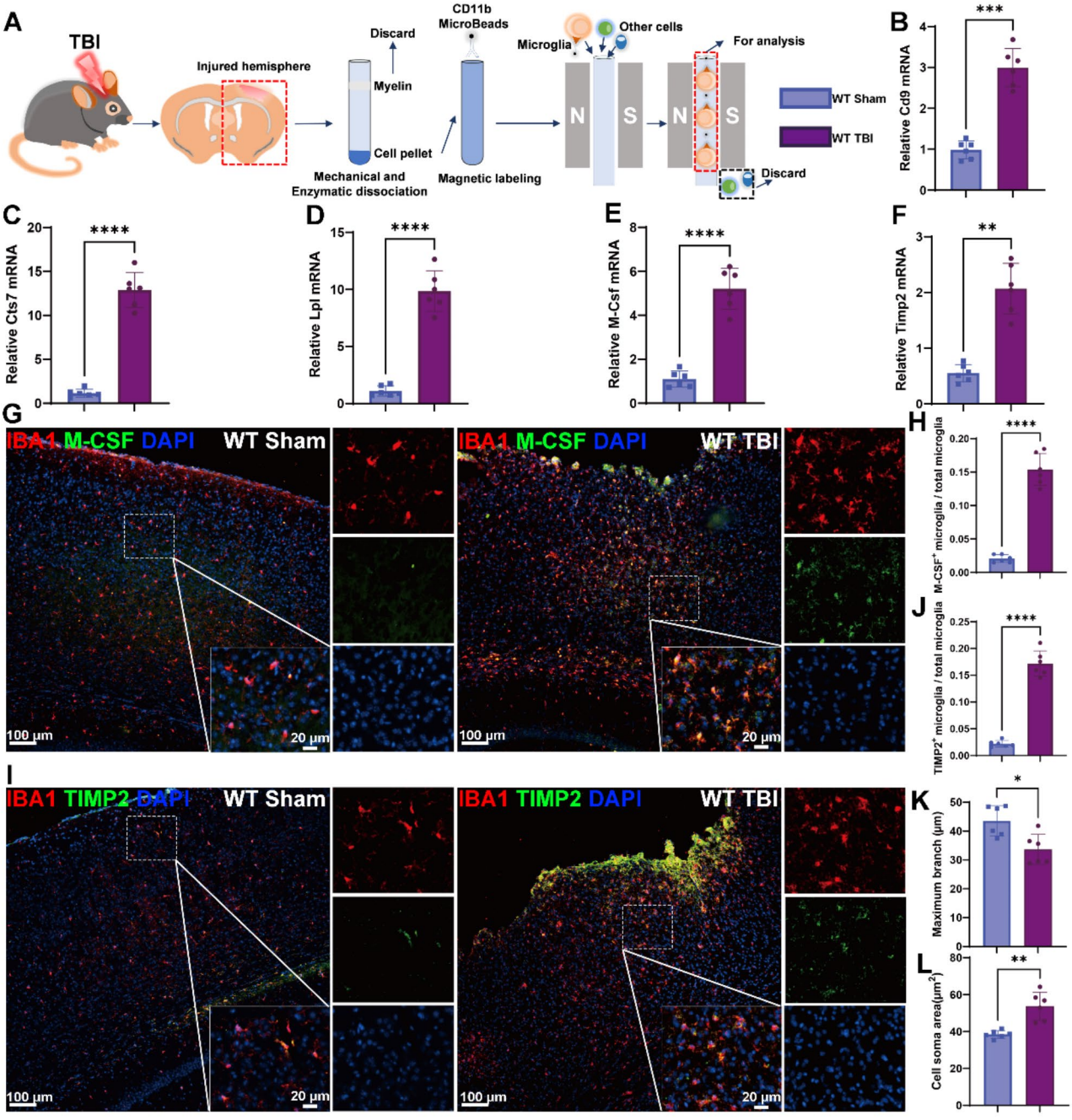

Fig. 1 Formation of DAM-like cells in mice during the acute phase of TBI. **A** A schematic outline of microglia sorting. **B-F** Relative DAM marker gene expression in microglia of Sham or TBI mice at 3 dpi. Selected DAM marker genes: Cd9 (**B**), Cst7 (**C**), Lpl (**D**), M-Csf (**E**), and Timp2 (**F**). Data are expressed as mean ± S.D. $^{**}P < 0.01$, $^{***}P < 0.001$, and $^{****}P < 0.0001$. $n = 6$ samples per group, each sample pooled from 3 mice brains. **G** Representative overlay images of IBA1/M-CSF/DAPI at the brain lesion of mice at 3 dpi (IBA1, red; M-CSF, green; DAPI, blue). Scale bar = 100 μm in representative images and Scale bar = 20 μm in enlarged images. **H** Quantitative analysis of M-CSF-positive microglia to total microglia in Sham and TBI mice at 3dpi. Data were expressed as mean ± S.D. $^{****}P < 0.0001$. $n = 6$ mice per group. **I** Representative overlay images of IBA1/TIMP2/DAPI in the brain lesion of mice at 3 dpi (IBA1, red; TIMP2, green; DAPI, blue). Scale bar = 100 μm in representative images and Scale bar = 20 μm in enlarged images. **J-L** Quantitative analysis of TIMP2-positive microglia to total microglia (**J**) and maximum branch length (**K**) and cell soma area (**L**) of microglia in Sham and TBI mice at 3dpi. Data were expressed as mean ± S.D. $^{*}P < 0.05$, $^{**}P < 0.01$, $^{****}P < 0.0001$. $n = 6$ mice per group

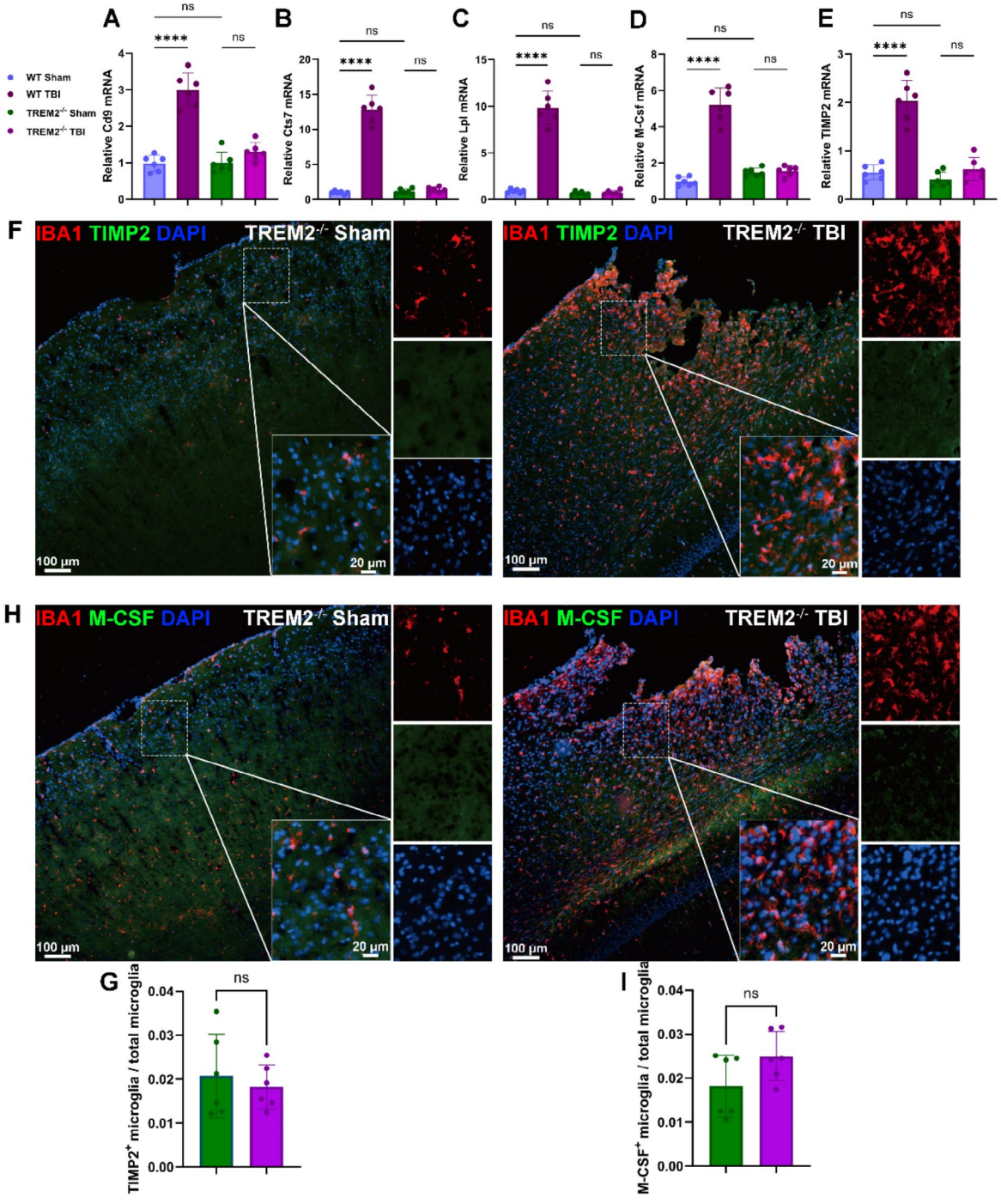

Fig. 2 TREM2 was required for the transformation of DAM-like cells in the acute phase of TBI in mice. **A-E** Bar plots showing expression of selected DAM marker genes Cd9 (**A**), Cst7 (**B**), Lpl (**C**), M-Csf (**D**) and Timp2 (**E**) in microglia from WT Sham, WT TBI, Trem2$^{-/-}$ Sham, and Trem2$^{-/-}$ TBI mice at 3 dpi. Data are expressed as the mean ± S.D. ****$P < 0.0001$. $n = 6$ samples per group, each sample pooled from 3 mice brains. **F** Representative images of a DAM marker protein (TIMP2, green), microglia marker protein (IBA-1, red), and cell nuclei (DAPI, blue) at lesion sites of TREM2$^{-/-}$ mice at 3dpi. Scale bar = 100 μm in representative images and Scale bar = 20 μm in enlarged images. **G** Quantitative analysis of TIMP2-positive microglia to total microglia in TREM2$^{-/-}$ Sham and TREM2$^{-/-}$ TBI mice at 3dpi. Data were expressed as mean ± S.D. $^{ns}P > 0.05$. $n = 6$ mice per group. **H** Representative images of a DAM marker protein (M-CSF, green), microglia marker protein (IBA-1, red), and cell nuclei (DAPI, blue) at lesion sites of TREM2$^{-/-}$ mice at 3dpi. Scale bar = 100 μm in representative images and Scale bar = 20 μm in enlarged images. **I** Quantitative analysis of M-CSF-positive microglia to total microglia in TREM2$^{-/-}$ Sham and TREM2$^{-/-}$ TBI mice at 3dpi. Data were expressed as mean ± S.D. $^{ns}P > 0.05$. $n = 6$ mice per group

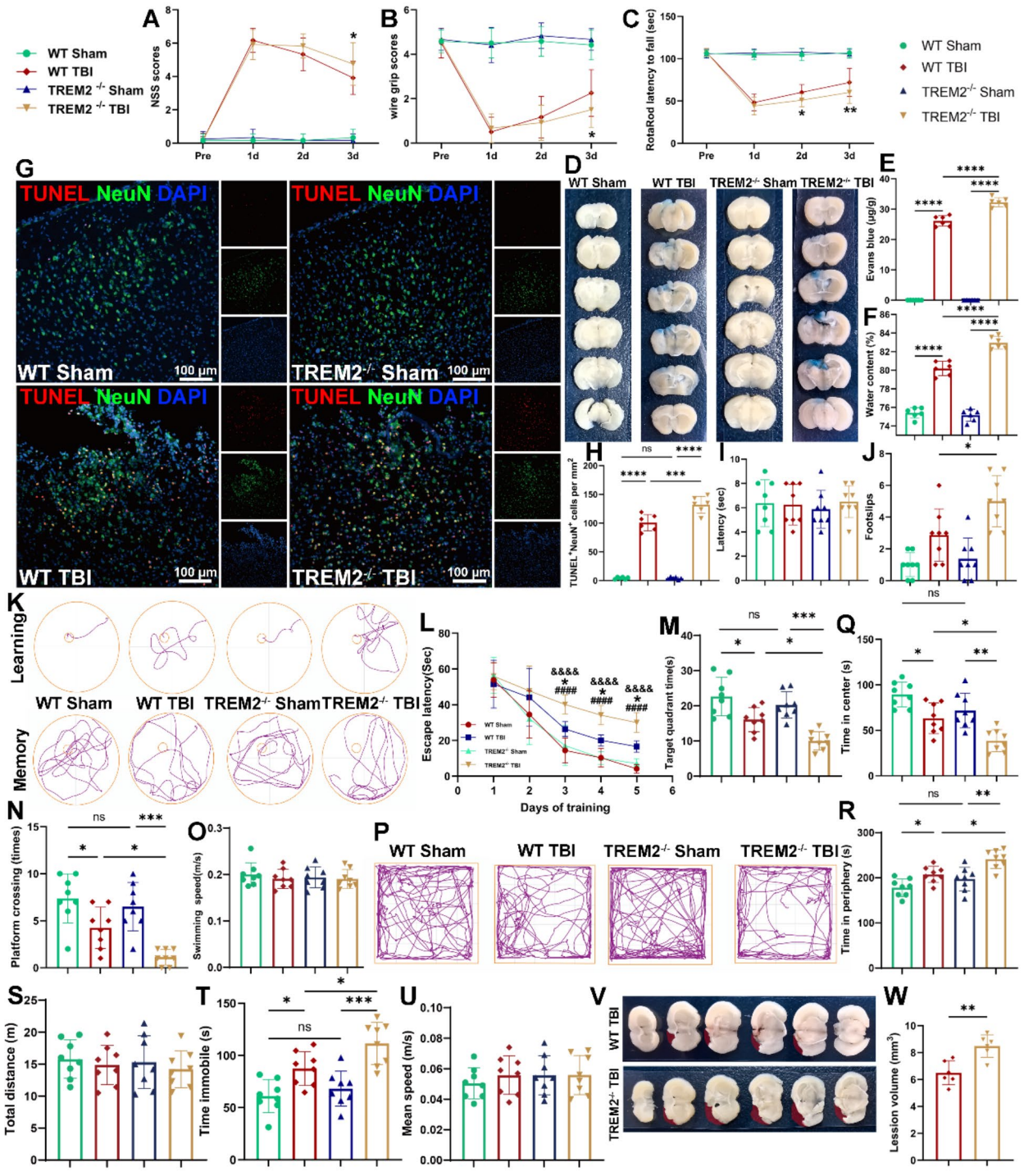

Fig. 3 (See legend on next page.)

abilities in TBI model mice, we conducted a Morris water maze test on days 15–20 post TBI. The escape latency served as a metric for assessing the learning ability of the mice. Our findings revealed that, compared with the Sham groups, the TBI groups exhibited prolonged escape latency during the learning trials on days 3–5 of training (Fig. 3K, L). Compared with WT TBI model mice, $TREM2^{-/-}$ TBI mice exhibited an even longer escape latency on days 3–5 of training (Fig. 3K, L), indicating poorer learning recovery in TREM2 knockout TBI mice. The time spent in the correct target quadrant and the number of crossings over the platform after its removal reflect the memory ability of the mice. Compared with the Sham groups, the TBI groups presented less time

(See figure on previous page.)

Fig. 3 TREM2 knockout impaired neurological recovery in TBI model mice. **A–C** Quantitative analysis of short-term neurological function by NSS scores (**A**), wire grip scores (**B**), and rotarod test (**C**). *$p < 0.05$ and **$p < 0.01$ vs. WT TBI, $n = 12$ mice per group. **D** Representative images of continuous coronal sections with Evans blue dye leakage for each group at 3 dpi. **E** Quantitative analysis of Evans blue leakage. The data are expressed as the means ± S.D. ****$P < 0.0001$. $n = 6$ mice per group. **F** Water content in brain tissue of each group at 3 dpi. The data are expressed as the means ± S.D. ****$P < 0.0001$. $n = 6$ mice per group. **G** Representative images of apoptosis neuron at the injured sites from WT and TREM2 KO mice at 3dpi. Scar bar = 100 μm. **H** Quantification of the number of TUNEL$^+$ NeuN$^+$ cells at the injured sites from WT and TREM2 KO mice at 3 dpi. The data are expressed as the means ± S.D. ***$P < 0.001$, ****$P < 0.0001$. $n = 6$ mice per group. **I**, **J** Quantitative analysis of motor function at 13 dpi by the beam walking test. The data are expressed as the means ± S.D. *$p < 0.05$, $n = 8$ mice per group. **K** Representative images of the swimming routes of mice in the Morris water maze. Up panel: Learning stage; down panel: Memory stage. **L** Latency to find the platform in the learning stage. The data are expressed as the means ± S.D. WT Sham vs. WT TBI: ###$P < 0.001$ and ####$P < 0.0001$; TREM2$^{-/-}$ Sham vs. TREM2$^{-/-}$ TBI: & &&&$P < 0.0001$; WT TBI vs. TREM2$^{-/-}$ TBI, *$P < 0.05$. $n = 8$ mice per group. **M-O** Quantitative analysis of the time in the target quadrant (**M**), the number of times crossing the platform (**N**) and the average swimming speed (**O**) in the probe trial. The data are expressed as the means ± S.D. *$P < 0.05$ and ***$P < 0.001$. $n = 8$ mice per group. **P** Representative images of the moving routes of mice in the open field test. **Q-U** Quantitative analysis of central time (**Q**), periphery time (**R**), total distance (**S**), time immobile (**T**), and mean speed (**U**) in the open field test. The data are expressed as the means ± S.D. *$P < 0.05$, **$P < 0.01$, and ***$P < 0.001$. $n = 8$ mice per group. **V** Representative images of injury size in WT and TREM2$^{-/-}$ TBI mice at 21 dpi. **W** Quantification of brain tissue loss in WT and TREM2$^{-/-}$ TBI mice at 21 dpi. The data are expressed as the means ± S.D. **$P < 0.01$. $n = 6$ mice per group

spent in the target quadrant and a reduced number of platform crossings (Fig. 3M, N). Compared with WT TBI model mice, TREM2$^{-/-}$ TBI model mice had even fewer target quadrant time and platform crossings (Fig. 3M, N). Furthermore, there was no statistical difference in swimming speed between all four groups in the memory stage (Fig. 3O).

TBI can cause anxiety-like behaviors in mice [41]. Mice naturally avoid the bright central area in an open field, so the percentage of time spent in the central area versus the peripheral area of the field can serve as a measure of anxiety-related behavior. Our experimental results demonstrated that, compared with the Sham groups, the TBI groups spent significantly less time in the central area, more time in the periphery and immobile, indicating anxiety-like behavior in the mice after TBI (Fig. 3P-R, and T). Furthermore, compared with WT TBI mice, TREM2$^{-/-}$ TBI mice exhibited more severe anxiety-like behavior (Fig. 3P-R, and T). In addition, there was no significant difference among the four groups in the total distance traveled and mean speed in the OFT (Fig. 3S, U). Finally, we conducted brain lesion size analysis after MWM were finished and found that TREM2 knockout hindered the repair of injured tissue (Fig. 3V, W). These behavioral and neuropathological findings collectively suggested TREM2 played a pivotal role in functional recovery after TBI and might has a close connection with DAM-like cells formation.

DAM-like cells assisted in clearing cellular debris and secreting repair-related cytokines

Previous studies have reported that microglia provide neuroprotection by engulfing cellular debris and secreting neurotrophic factors such as BDNF and VEGFa [42–44]. Therefore, we hypothesized that the impaired transformation of DAM-like cells in TREM2 knockout TBI model mice may lead to their inability to execute such neuroprotective functions. Prompt clearance of cellular debris after TBI reduces inflammation and is the basis for later neural reconstruction and recovery [22]. Initially, we aimed to determine whether DAM-like cells are involved in clearing cellular debris in TBI model mice. Through triple immunofluorescence staining of neuronal debris with NeuN and DAM with IBA1 and TIMP2, we observed the accumulation of granular neuronal debris in DAM-like cells (IBA1$^+$ TIMP2$^+$) in the brains of mice at 3 dpi (Fig. 4A). Meanwhile, the statistical analysis results indicated that DAM-like cells engulfed significantly more neuronal debris than non-DAM cells (Fig. 4B), and TREM2 knockout significantly reduced the overall ability of microglia to engulf neuronal debris (Fig. 4A, C), suggesting that DAM-like cells might promote neurofunctional recovery by clearing cellular debris.

Neurotrophic factors secreted by microglia, such as BDNF, play crucial roles in regulating cellular homeostasis [42]. Additionally, increased expression of microglial BDNF may lead to increased survival of intermediate neurons after TBI, thereby maintaining the process of neurodegeneration and contributing to improvements in cognitive ability [42]. Hence, we aimed to investigate whether DAM-like cells can secrete BDNF. We measured the expression of BDNF in the DAM-like cells of the mice at 3 dpi. Our immunofluorescence staining results revealed the colocalization of BDNF and DAM-like cells, and the expression of BDNF in DAM cells was significantly higher than that in non-DAM cells (Fig. 4D, E). Furthermore, Western blot results showed that at the tissue level, the expression of BDNF was significantly reduced after TBI, and TREM2 knockout further reduced its expression (Fig. 4F, G). Moreover, vascular endothelial growth factor A (VEGFa) is a crucial regulator of vascular health, promoting brain recovery after severe damage [45]. Immunofluorescence staining revealed the colocalization of VEGFa and DAM-like cells in the brains of model mice at 3 dpi, and the expression of VEGFa in DAM cells was significantly higher than that in non-DAM cells (Fig. 4H, I). Furthermore, Western blot results showed that at the tissue level, the expression of VEGFa

was significantly increased after TBI, however, TREM2 knockout reduced its expression when compared to the WT TBI mice (Fig. 4J, K). RT–qPCR analysis of DAM-like cells and non-DAM microglia isolated via magnetic beads (Fig. 4L) confirmed a significant increase in BDNF mRNA levels compared with those in non-DAM microglia (Fig. 4M). Furthermore, compared with non-DAM microglia, DAM-like cells presented significant VEGFa mRNA upregulation (Fig. 4N).

In summary, the clearance of cellular debris and secretion of cytokines by DAM-like cells may partially contribute to the promotion of recovery in mice following TBI.

Enhanced glycolysis in the DAM-like cells of TBI model mice at 3 dpi

Given the important role of glycolysis in microglial phenotypic transformation, we aimed to elucidate the glucose metabolic status of DAM-like cells in the acute phase of TBI in mice. We examined the expression of the key glycolytic enzyme PKM2 in DAM-like cells via immunofluorescence staining. The data revealed a marked upregulation of PKM2 expression in DAM-like cells in the TBI group compared with microglia in the Sham group (Fig. 5A, B). The fluorescent D-glucose analogue (2-NBDG) reflects the glycolytic capability in vivo. Following the protocol outlined in the literature, the mice were administered 2-NBDG intravenously via the tail vein, and subsequent brain tissue was obtained for subsequent immunofluorescence staining [33]. Our investigation revealed that, in comparison with microglia in the Sham group, there was a notably greater accumulation of 2-NBDG in DAM-like cells in the TBI group at 3 dpi (Fig. 5C, D), which was indicative of the increased glucose uptake by DAM-like cells and their increased glycolytic activity.

To further validate these results in vivo, we investigated glycolysis in DAM-like cells isolated from mice at 3 dpi. Leveraging single-cell dissociation techniques in conjunction with magnetic beads coated with an anti-CD11c antibody, we isolated active DAM-like cells ($CD11c^+$) for culture in vitro to subsequently investigate the characteristics and functions of these cells. We evaluated the glycolysis and glycolytic capacity of DAM-like cells in the brains of mice at 3 dpi by dynamically measuring the ECAR. Under glucose-deprived conditions, DAM-like cells and microglia derived from the Sham group were exposed to glucose sequentially to determine the baseline glycolytic activity of the cells. Glycolytic capacity was assessed by stimulating glycolysis via the ATP synthase inhibitor oligomycin. Compared with microglia in Sham group, both glycolysis and glycolytic capacity were significantly increased in DAM-like cells (Fig. 5E-G). Additionally, using magnetic beads, we isolated and cultured microglia and DAM-like cells, followed by treatment with 2-NBDG. The findings revealed a significant increase in the fluorescence intensity of DAM-like cells compared with that of Sham microglia (Fig. 5H, I), which were consistent with the in vivo results. To further corroborate these findings, our RT-qPCR results showed that the transcription levels of glucose transporter 1 and 5 (GLUT1 and GLUT5) were significantly higher in DAM cells than in microglia of Sham group (Fig. 5J, K). Furthermore, our observations revealed that, compared with microglia from the Sham group, DAM-like cells from the TBI group at 3 dpi presented an approximately 40–60% increase in glucose consumption and a 30–50% increase in lactate production (Fig. 5L, M). These collective findings underscored the enhanced glycolysis in DAM-like cells during the acute phase of TBI in mice.

TREM2 knockout impaired microglial glycolytic activation and the AKT/mTOR/HIF1α signalling pathway during the acute phase of TBI in mice

We intravenously injected 2-NBDG into the tail vein of mice at 3 dpi and subsequently performed immunofluorescence staining on the brain tissue sections of the mice. The results revealed a statistically significant decrease in 2-NBDG uptake by microglia in $TREM2^{-/-}$ mice compared with WT mice at 3 dpi (Fig. 6A, B). To corroborate these results in vivo, we conducted real-time measurements of the ECAR in microglia isolated from WT and $TREM2^{-/-}$ mice at 3 dpi. Our analysis demonstrated that glycolysis and the glycolytic capacity of microglia were lower in TREM2-knockout mice than in WT mice (Fig. 6D-E). Moreover, we measured lactate production and glucose consumption in microglia isolated from mice at 3 dpi. Compared with those in the Sham group, microglial cells from both the WT and $TREM2^{-/-}$ mice groups presented increased lactate production and glucose consumption at 3 dpi, but compared to those from the WT TBI group, microglia from the $TREM2^{-/-}$ TBI group presented decreased lactate production and glucose consumption, suggesting a reduction in glycolysis (Fig. 6F, G). Moreover, there was no statistically significant difference between the WT Sham and $TREM2^{-/-}$ Sham groups.

To further elucidate the underlying mechanisms of the impact of TREM2 on glucose metabolism in microglia in the context of TBI, we conducted Western blot analyses on the brain tissues from either TREM2 knockout mice or mice treated with the TREM2 agonist COG1410. Previous studies have shown the pivotal role of the AKT/mTOR/HIF1α signalling pathway in energy metabolism in microglia [46]. To determine the involvement of the AKT/mTOR/HIF1α pathway in TREM2-mediated metabolic reprogramming after TBI, we assessed the AKT-mTOR-HIF1α pathway in WT and $TREM2^{-/-}$ mice subjected to TBI or treated with the TREM2 agonist

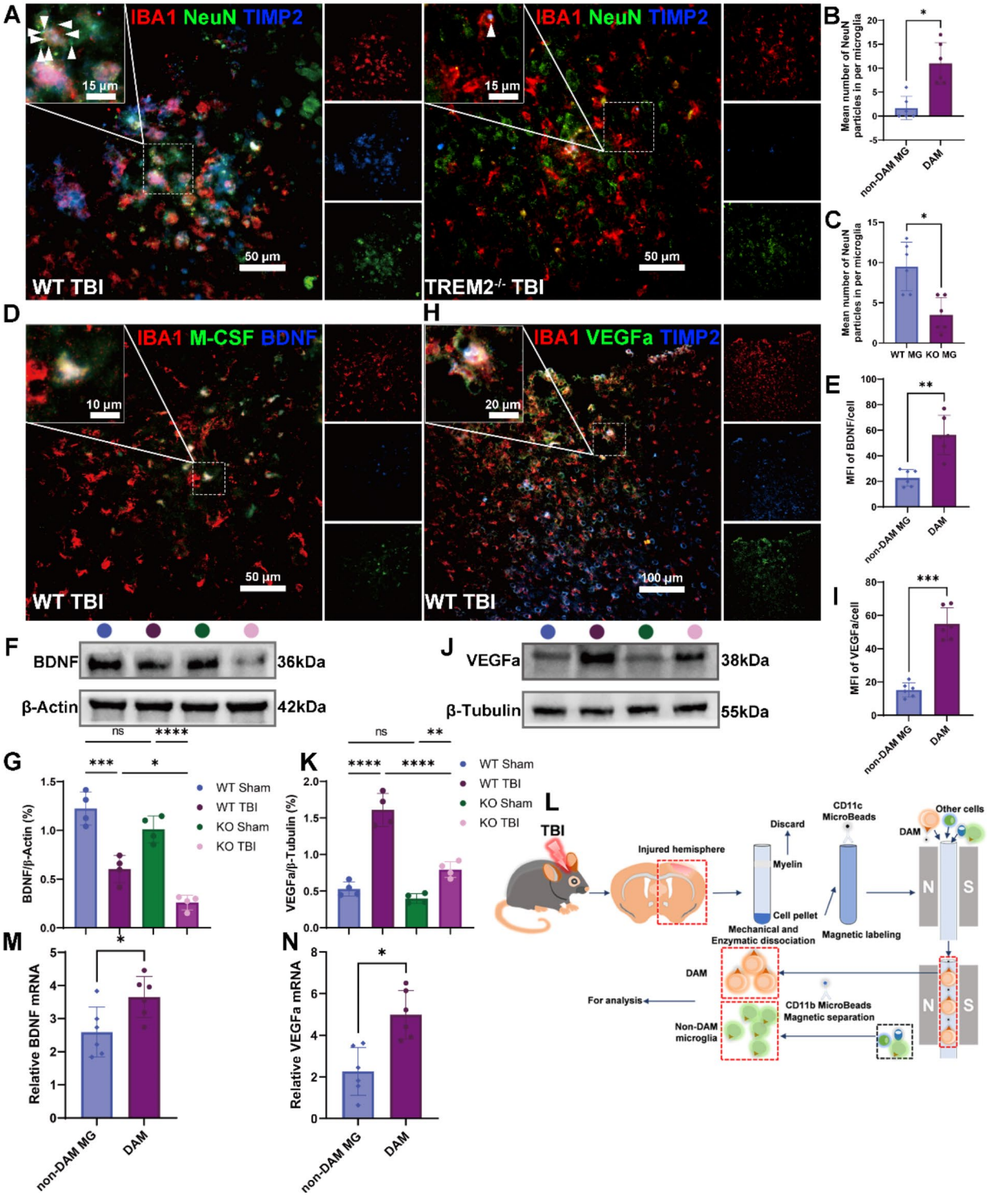

Fig. 4 (See legend on next page.)

COG1410. Our findings revealed a reduction in HIF-1α expression and activation of the AKT/mTOR signaling axis in TREM2-knockout mice with TBI, compared with WT TBI mice. Conversely, the treatment of TBI model mice with a TREM2 agonist for 24 h resulted in elevated levels of phosphorylated AKT and mTOR, accompanied by the upregulation of HIF-1α. However, in TREM2$^{-/-}$ TBI model mice treated with the TREM2 agonist, there was no significant increase in the levels of phosphorylated AKT, mTOR, or HIF-1α (Fig. 6H-K).

(See figure on previous page.)

Fig. 4 DAM-like cells assisted in clearing cellular debris and secreting repair-related cytokines. **A** Representative images of neural debris in DAM-like microglia at 3 dpi. Neurons are labeled with NeuN (green) and DAM-like microglia are labeled with TIMP2 (blue) and IBA-1 (red). The white arrows represent neural debris. Scale bar = 50 μm in representative images and Scale bar = 15 μm in enlarged images. **B** Quantification of the neuron debris engulfment by DAM-like microglia and non-DAM microglia at 3 dpi. The data are expressed as the means ± S.D. $^{*}P < 0.05$. $n = 6$ mice per group. **C** Quantification of the neuron debris engulfment by microglia of WT and TREM2$^{-/-}$ TBI mice at 3 dpi. The data are expressed as the means ± S.D. $^{*}P < 0.05$. $n = 6$ mice per group. **D** Representative brain sections from WT TBI mice at 3 dpi showing DAM-like cells secreting BDNF (blue). DAM cells are stained by M-CSF (green) and microglia are stained by IBA-1 (red). Scale bar = 50 μm in representative images and Scale bar = 10 μm in enlarged images. **E** Quantification of the mean fluorescence intensity (MFI) of BDNF in DAM-like and non-DAM microglia in WT TBI mice at 3 dpi. The data are expressed as the means ± S.D. $^{**}P < 0.01$. $n = 6$ mice per group. **F** Western blot bands of BDNF and β-Actin in WT and TREM2$^{-/-}$ TBI mice at 3 dpi. β- Actin was used as a loading control. **G** Quantitative analysis of BDNF protein expression in the WT sham, WT TBI, TREM2$^{-/-}$ Sham, and TREM2$^{-/-}$ TBI mice at 3 dpi. Data represent mean ± S.D. $^{*}p < 0.05$, $^{***}p < 0.001$, $^{****}p < 0.0001$. $n = 4$ mice per group. **H** Representative brain sections from WT TBI mice at 3 dpi showing DAM-like cells secreting VEGFa (green). DAM cells are stained by TIMP2 (blue) and microglia are stained by IBA-1 (red). Scale bar = 100 μm in representative images and Scale bar = 20 μm in enlarged images. **I** Quantification of the MFI of VEGFa in DAM-like and non-DAM microglia in WT TBI mice at 3 dpi. The data are expressed as the means ± S.D. $^{***}P < 0.001$. $n = 6$ mice per group. **J** Western blot bands of VEGFa and β-Actin in WT and TREM2$^{-/-}$ TBI mice at 3 dpi. β- Actin was used as a loading control. **K** Quantitative analysis of VEGFa protein expression in the WT sham, WT TBI, TREM2$^{-/-}$ Sham, and TREM2$^{-/-}$ TBI mice at 3 dpi. Data represent mean ± S.D. $^{**}p < 0.01$, $^{****}p < 0.0001$. $n = 4$ mice per group. **L** A schematic outline of DAM-like and non-DAM microglia sorting. **M**, **N** Relative BDNF (**M**) and VEGFa (**N**) mRNA expression in DAM-like and non-DAM microglia sorted from WT TBI mice at 3 dpi. The data are expressed as the means ± S.D. $^{*}P < 0.05$. $n = 6$ samples per group, each sample pooled from the brains of 3 mice

Inhibition of glycolysis impeded the transformation of DAM-like cells in TBI model mice at 3 dpi

To investigate the impact of glycolysis inhibition on the transformation of TBI-induced DAM-like cells, we inhibited glycolysis in TBI model mice to observe changes in the proportion of DAM-like cells. The mice were intraperitoneally injected with 2-DG (400 mg/kg/d) before and after TBI. Brain tissue from mice was collected at 3 dpi for double immunofluorescence staining with M-CSF or TIMP2 and IBA1 to evaluate the effects of glycolysis inhibitors on the transformation of DAM-like cells in mice after TBI. Following 2-DG administration, the proportions of microglia co-stained with M-CSF or TIMP2 in WT TBI + 2-DG group was significantly decreased than that in the WT TBI + Vehicle group (Fig. 7A-D). To quantitatively assess the impact of 2-DG on DAM transformation, microglia from TBI model mice treated with or without 2-DG were isolated (Fig. 7E), and flow cytometry was used to evaluate the changes in the proportion of DAM-like cells. Flow cytometry analysis revealed that 2-DG treatment reduced the proportion of DAM-like cells in mice at 3 dpi (Fig. 7F, G). Furthermore, RT–qPCR analysis confirmed that the mRNA expression of the DAM marker genes Timp2, M-Csf, Lpl, Cd9, and Cst7 was lower in microglia from 2-DG-treated mice than in those from untreated mice at 3 dpi (Fig. 7H-L). Overall, these findings supported the conclusion that the transformation of microglia into DAM-like cells in the acute phase of TBI in mice was regulated by glycolytic metabolism.

Enhanced glycolysis partially restored the DAM-like phenotype in microglia and neurological function in TREM2$^{-/-}$ TBI model mice

Our data suggest that glycolysis regulates the transformation of DAM-like cells in TBI mice and that the glycolytic dysfunction induced by TREM2 knockout partially impedes DAM transformation. Therefore, we hypothesized that enhancing glycolysis could partially reverse the impairment of DAM-like cell transformation after TBI in TREM2$^{-/-}$ mice. Fructose-1,6-bisphosphate trisodium salt (FBP) is a glycolysis enhancer that is considered responsible for maintaining glycolysis and increasing ATP production as a high-energy endogenous intermediate in the glycolytic pathway [31]. To test our hypothesis, TREM2$^{-/-}$ TBI model mice were intraperitoneally injected with FBP trisodium salt at a dosage of 500 mg/kg/day before and after TBI. Brain tissue from mice was collected at 3 dpi for double immunofluorescence staining with the key enzyme of glycolysis, Pyruvate kinase isozyme type M2 (PKM-2) and the microglial cell marker IBA1 to assess whether microglial glycolysis was enhanced by FBP. Our results showed that PKM-2 was significantly increased in FBP treated microglia compared to non-treated microglia, indicating enhanced glycolysis (Fig. 8A, B). Furthermore, double immunofluorescence staining with the DAM markers M-CSF or TIMP2 and the microglial marker IBA1 revealed that the administration of FBP increased the proportion of DAM-like cells (Fig. 8C-F).

Additionally, microglia from TREM2$^{-/-}$ mice treated with or without FBP were isolated at 3 dpi, and flow cytometry was used again to quantitatively measure the proportion of DAM-like cells, revealing that FBP treatment increased the proportion of DAM-like cells in TREM2$^{-/-}$ mice at 3 dpi (Fig. 8G, H). RT-qPCR analysis of DAM marker gene expression revealed that FBP treatment partially restored the expression of DAM marker genes (Cd9, Cst7, Lpl, M-Csf, and Timp2) in microglia from TREM2$^{-/-}$ mice at 3 dpi (Fig. 8I-M). These findings further supported the notion that glycolysis plays a role in the transformation of DAM-like cells.

Furthermore, we investigated whether treatment with FBP improves the neurological function

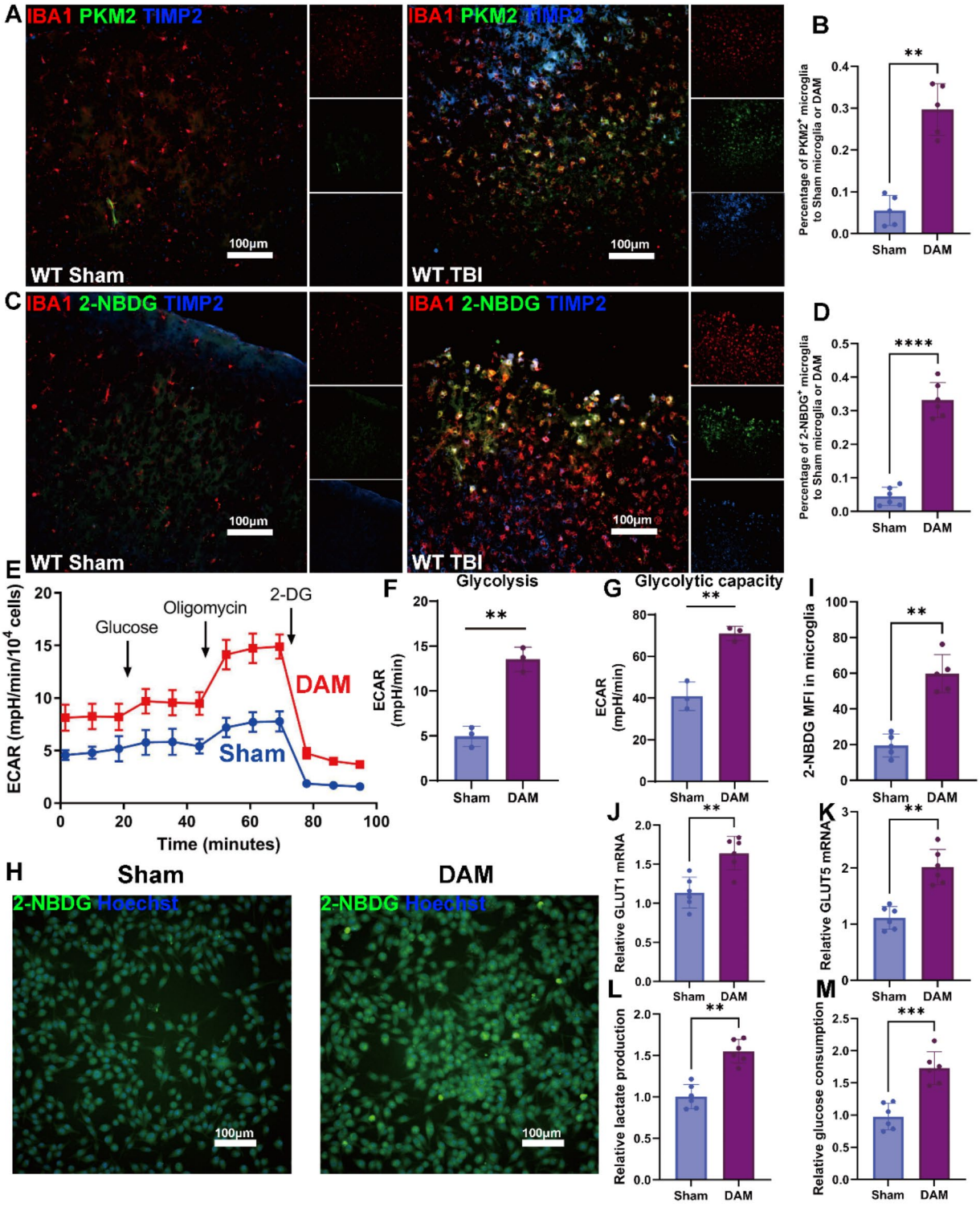

Fig. 5 (See legend on next page.)

of TREM2$^{-/-}$ TBI model mice. Compared with the TREM2$^{-/-}$ TBI + Vehicle group, the TREM2$^{-/-}$ TBI + FBP group had significantly lower NSS score (Fig. 9A) and increased wire grip scores (Fig. 9B) and rotarod latency on days 3 after TBI (Fig. 9C). Next, neuropathological observations suggested that FBP treatment alleviated BBB damage and brain edema in TREM2 knockout mice with TBI (Fig. 9D-F). On days 13 post-TBI, we

(See figure on previous page.)

Fig. 5 Enhanced glycolysis in the DAM-like cells of TBI model mice at 3 dpi. **A** Representative images of PKM2 (green) in microglia of WT Sham mice and DAM-like cells of TBI mice at 3 dpi, labeled with TIMP2 (blue) and IBA-1 (red). Scale bar = 100 μm. **B** Quantitative analysis of the $PKM2^+$ cells in microglia of Sham mice and DAM-like cells of TBI mice. The data are expressed as the mean ± S.D. $^{**}p < 0.01$. $n = 6$ mice per group. **C** Representative images of 2-NBDG (green) uptake in microglia of Sham mice and DAM-like cells of TBI mice at 3 dpi, labeled with TIMP2 (blue) and IBA-1 (red). Scale bar = 100 μm. **D** Quantitative analysis of the 2-NBDG^+ cells in microglia of Sham mice and DAM-like cells of TBI mice. The data are expressed as the mean ± S.D. $^{****}P < 0.0001$. $n = 6$ mice per group. **E-G** Microglia from Sham mice and DAM-like cells ($CD11c^+$) from WT TBI mice at 3 dpi were supplied with 10 mM glucose, 2 μM oligomycin, and 100 mM 2-DG at the indicated times. ECAR was examined using Seahorse XFe24 analyzer (**E**). Relative glycolysis levels (**F**) and glycolytic capacity (**G**) are normalized to the cell number. The data are expressed as the mean ± S.D. $^{**}p < 0.01$. $n = 3$ samples per group, each sample pooled from 5 mouse brains. **H** Representative images of 2-NBDG (green) uptake in microglia sorted from Sham mice and DAM-like cells from WT TBI mice at 3 dpi. scale bar = 100 μm. **I** Quantitative analysis of 2-NBDG MFI in microglia. The data are expressed as the mean ± S.D. $^{**}P < 0.01$. $n = 5$ samples per group, each sample pooled from 3 mouse brains. **J**, **K** Relative GLUT1 and GLUT5 mRNA expression in microglia sorted from sham mice and DAM-like cells from WT TBI mice at 3 dpi. Data are presented as the mean ± S.D. $^{**}P < 0.01$. $n = 6$ samples per group, each sample pooled from the brains of 3 mice. **L**, **M** Lactate excretion (**L**) and glucose consumption (**M**) of microglia sorted from Sham mice and DAM-like cells from WT TBI mice at 3 dpi. Data are mean ± S.D. $^{**}P < 0.01$ and $^{***}P < 0.001$. $n = 6$ samples per group, each sample pooled from 3 mouse brains

subsequently conducted the beam walking test to evaluate motor function. We found no significant difference in the latency to traverse the beam between the $TREM2^{-/-}$ TBI + Vehicle and $TREM2^{-/-}$ TBI + FBP groups of mice (Fig. 9G). However, FBP treatment reduced the number of footslips (Fig. 9H). Following this, from days 15 to 20 post-TBI, spatial learning and memory function were evaluated via the Morris water maze. Compared with $TREM2^{-/-}$ TBI + Vehicle treatment, FBP treatment significantly reduced escape latency in the place navigation test during the learning phase (Fig. 9I, J). In the memory test phase, FBP treatment enhanced both the time spent in the target quadrant and the number of platform crossings in $TREM2^{-/-}$ TBI model mice (Fig. 9K, L). There was no statistical difference in swimming speed between $TREM2^{-/-}$ TBI model mice treated with or without FBP (Fig. 9M). Next, open field testing was performed on days 21 post TBI to assess anxiety-like behavior. Our findings indicated that, compared with vehicle, FBP treatment alleviated anxiety-like behavior in $TREM2^{-/-}$ TBI model mice, increasing the time spent in the center and decreasing the time in the periphery and immobile (Fig. 9N-P, and R). There was no significant difference among the two groups in the total distance traveled and mean speed in the OFT (Fig. 9Q, S). Finally, brain lesion size analysis after MWM demonstrated that FBP treatment improved the repair of injured tissue (Fig. 9T, U).

Discussion

Our study provides a detailed investigation into the potential roles of DAM-like cells in the acute phase of TBI in mice, with a particular focus on the glycolytic status and potential functions of DAM-like cells. We elucidated the regulatory role of glycolysis in DAM-like cell transformation and several of the molecular mechanisms involved in the acute phase of TBI in mice. Microglia, which play crucial roles in the central nervous system, have emerged as attractive targets for treating neurological disorders. However, a deeper understanding of microglial diversity and dynamics is essential for developing effective strategies for manipulating microglia. Most microglia remain in a resting state under physiological conditions and become activated and proliferate following tissue injury [47, 48]. The classical binary classification of microglia activation into proinflammatory and anti-inflammatory phenotypes is too simplistic to capture the complex physiological roles that microglia play in neurologic diseases [49]. Microglia can currently be distinguished based on the expression of specific genes [50], representing different functional states [51], which assign transcriptional identities to microglia and can change depending on local or environmental signals.

The use of novel high-throughput sequencing technologies and single-cell methods combined with epigenetic analysis to detect the expression profiles of microglia has revealed multiple previously unknown subtypes, including a unique DAM subset. DAM have been observed in various diseases, such as ageing, AD [5], MS [7], neurodegenerative diseases [52], inflammation [53], demyelinating diseases [54], and neuronal apoptosis [7]. The presence of DAM in many diseases indicates that it is an important subtype of microglia, and its transformation is dependent on TREM2-APOE signalling [5, 7]. However, the mechanism by which the DAM phenotype arises remains unclear. Furthermore, most studies on DAM have focused on chronic diseases, and their role in acute TBI is still not understood. Moreover, nearly all previous TBI studies have used whole-brain tissue to infer the response of microglia to injury [55], which may not reflect specific changes in microglial gene expression. By using single-cell sorting technology, we isolated microglia from mice at 3 dpi for immunofluorescence analysis, which revealed the expression of signature genes of DAM-like cells and confirmed the presence of DAM-like cells in the acute phase of TBI in these mice. These findings suggest that microglia can transform into a DAM-like state during the acute phase of TBI, like that in chronic neurological diseases, indicating a potentially important role of DAM-like cells in the acute phase of TBI.

TREM2 is a membrane protein whose expression increases in neurological diseases, and our previous

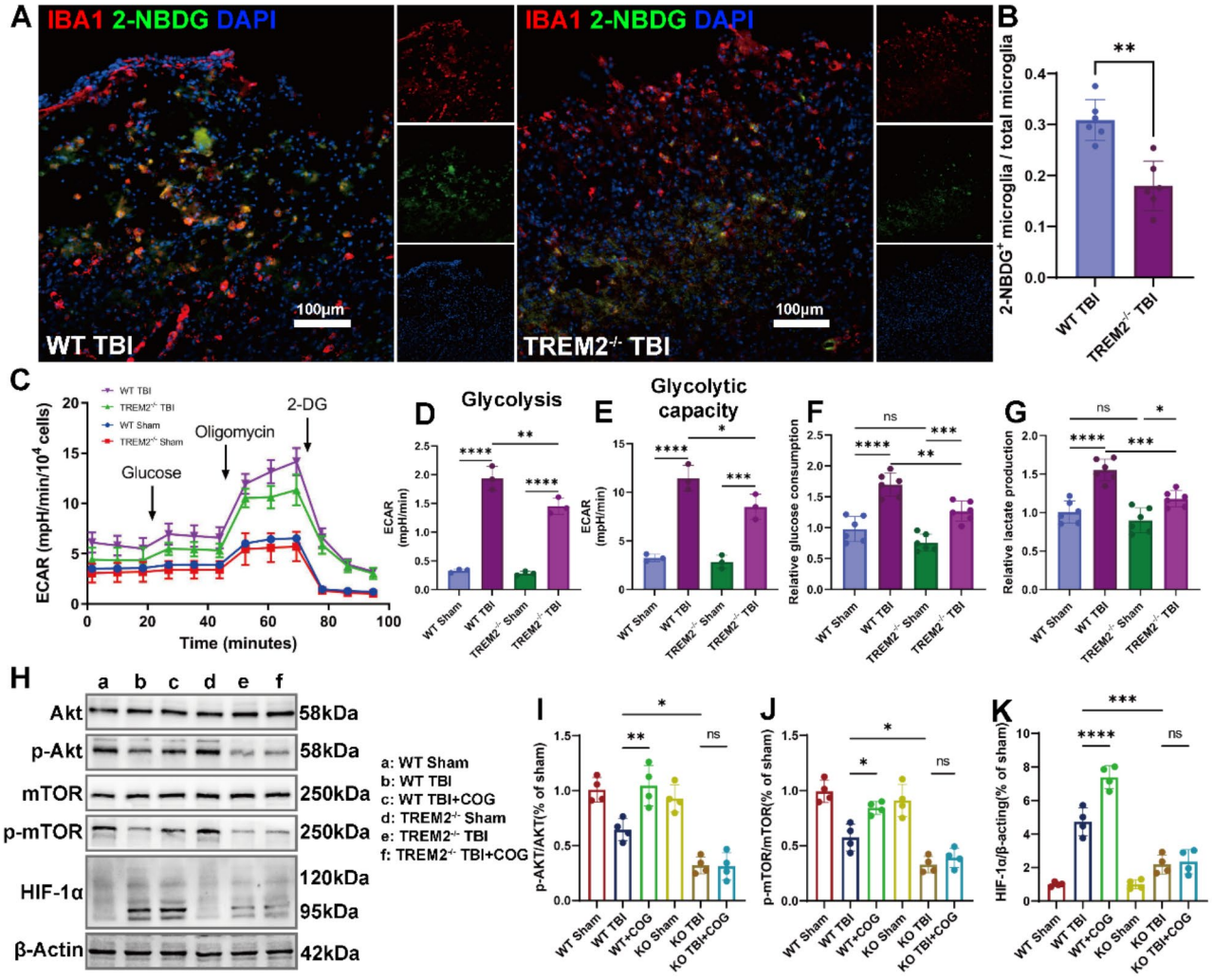

Fig. 6 TREM2 knockout impaired microglial glycolytic activation and the AKT/mTOR/HIF1α signalling pathway during the acute phase of TBI in mice. **A** Representative images of 2-NBDG uptake in microglia of WT and TREM2$^{-/-}$ TBI mice at 3 dpi. Scale bar = 100 μm. **B** Quantitative analysis of 2-NBDG^{+} positive microglia to total microglia in WT and TREM2$^{-/-}$ TBI mice at 3 dpi. The data are expressed as the mean ± S.D. $^{**}P < 0.01$. $n = 6$ mice per group. **C-E** Microglia from WT sham mice, WT TBI mice, TREM2$^{-/-}$ Sham mice, and TREM2$^{-/-}$ TBI mice at 3 dpi were supplied with 10 mM glucose, 2 μM oligomycin, and 100 mM 2-DG at the indicated times. ECAR was examined using the Seahorse XFe24 analyzer (**C**). Relative glycolysis levels (**D**) and glycolytic capacity (**E**) are normalized to the cell number (mean ± S.D. $^{*}p < 0.05$, $^{**}p < 0.01$, $^{***}p < 0.001$, and $^{****}p < 0.0001$. $n = 3$ samples per group, each sample pooled from 5 mice brains). **F**, **G** Relative glucose consumption and lactate production of microglia sorted from WT sham mice, WT TBI mice, TREM2$^{-/-}$ sham mice, and TREM2$^{-/-}$ TBI mice at 3dpi. Data represent mean ± S.D. $^{*}p < 0.05$, $^{**}p < 0.01$, $^{***}p < 0.001$, and $^{****}p < 0.0001$. $n = 6$ samples per group, each sample pooled from 3 mouse brains. **H-K** Western blot analysis of AKT-mTOR pathway components and HIF-1α in WT and TREM2$^{-/-}$ TBI mice treated with TREM2 agonist COG1410. β-Actin was used as a loading control (**H**). Quantitative analysis of p-Akt (**I**), p-mTOR (**J**), and HIF-1α (**K**) protein density. Data represent mean ± S.D. $^{*}p < 0.05$, $^{**}p < 0.01$, $^{***}p < 0.001$, and $^{****}p < 0.0001$. $n = 4$ mice per group

experiments demonstrated that TREM2 expression also increased following TBI. Knocking out TREM2 in mice can block the transformation of DAM [56]. The loss of TREM2 function maintains microglia in a resting state [57]. We found that TREM2 knockout also affects the transformation of microglia into mature DAM-like cells after TBI in mice. In TREM2$^{-/-}$ mice at 3 dpi, the expression of DAM signature genes was hindered, preventing homeostatic microglia from transforming into mature DAM and potentially affecting the proper function of the DAM in acute brain injury and TBI recovery. Additionally, our behavioural experiments in TBI model mice revealed TREM2 knockout-induced impairments in memory and learning ability, and anxiety-like behaviours in mice with inhibited transformation of DAM-like cells. However, the effect of TREM2 deletion on motor function was minimal, in contrast to the more pronounced effect on cognition. After a 3-day balance beam training prior to TBI, the formal balance beam test was performed on days 13 post-TBI. The results were consistent with our

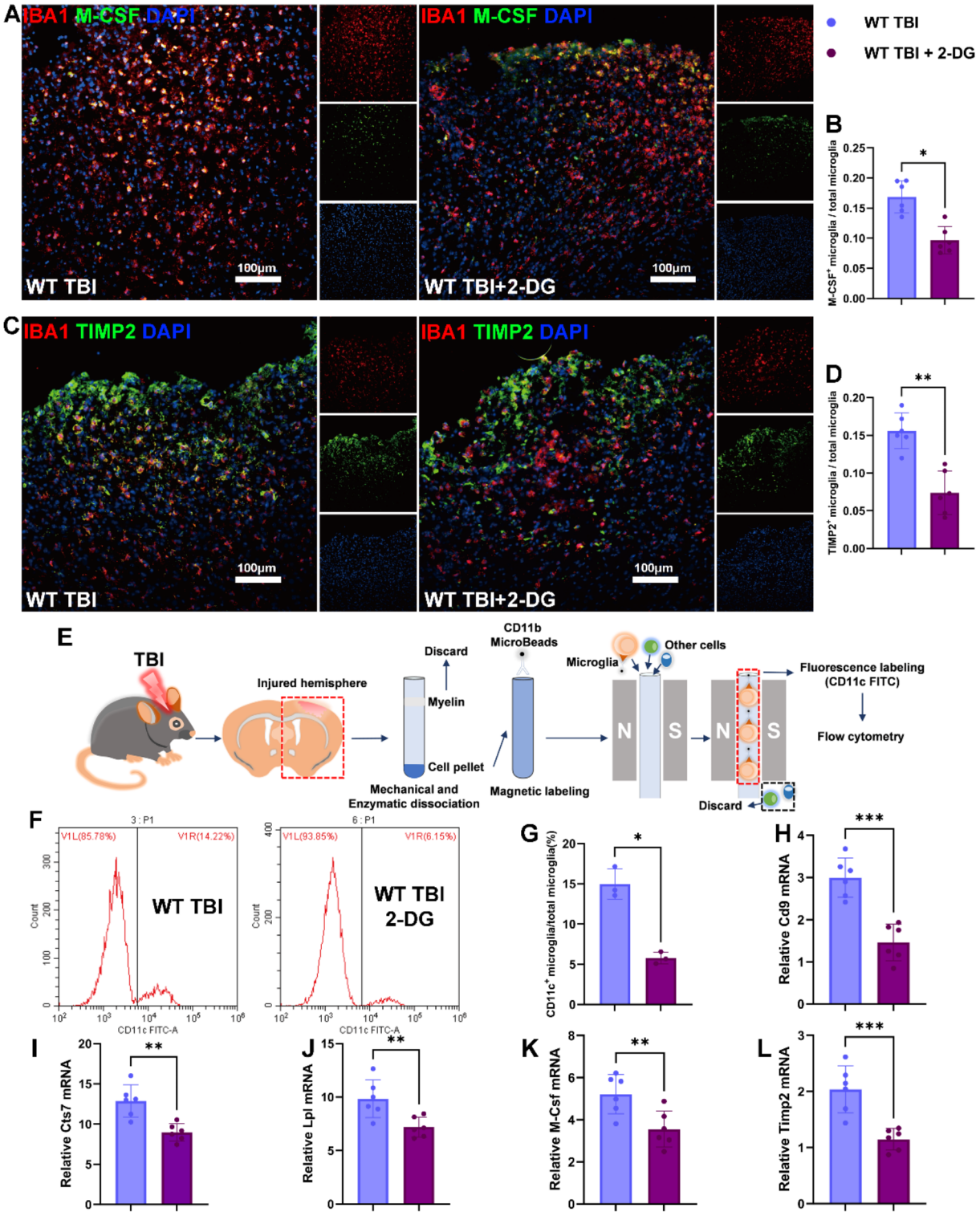

Fig. 7 (See legend on next page.)

(See figure on previous page.)

Fig. 7 Inhibition of glycolysis impeded the transformation of DAM-like cells in TBI model mice at 3 dpi. **A** Double immunofluorescence staining for M-CSF (green) and IBA1 (red) in the cortex of WT TBI mice at 3 dpi, treated with or without 2-DG. Scale bar = 100 μm. **B** Quantitative analysis of M-CSF$^+$ microglia to total microglia. The data are expressed as mean ± S.D. *$P < 0.05$. $n = 6$ mice per group. **C** Double immunofluorescence staining for TIMP2 (green) and IBA1 (red) in the cortex of WT TBI mice at 3 dpi, treated with or without 2-DG. Scale bar = 100 μm. **D** Quantitative analysis of TIMP2$^+$ microglia to total microglia. The data are expressed as mean ± S.D. **$P < 0.01$. $n = 6$ mice per group. **E** Diagram illustrating the proportion of DAM-like cells detected by flow cytometry. **F** Representative images of flow cytometric analysis depicting the proportion of CD11c$^+$ (a DAM marker) cells in microglia (CD11b$^+$) from the brains of WT TBI mice at 3 dpi treated with or without 2-DG. **G** Quantitative analysis of CD11c$^+$ cells to total microglia (CD11b$^+$). Data are represented as the mean ± S.D. *$P < 0.05$. $n = 3$ mice per group. **H-L** The relative mRNA expression of Cd9 (**H**), Cst7 (**I**), Lpl (**J**), M-Csf (**K**), and Timp2 (**L**) in microglia sorted from WT TBI mice at 3 dpi, treated with or without 2-DG. Data are presented as the mean ± S.D. **$p < 0.01$, ***$p < 0.001$. $n = 6$ samples per group, each sample pooled from 3 mice brains

previous study [24], in which mice were able to traverse the beam quickly, but TREM2 knockout led to more footslips. The open field test (total distance) and water maze test (swimming speed) both indicated that the overall motor function of both WT and TREM2 knockout mice could recover well during the chronic phase post-TBI. Previous studies have also shown that animals experienced balance impairment and a lack of postural orientation after TBI [58]. Therefore, TREM2 knockout might not affect the time taken to cross the beam but increase the frequency of fine motor errors in mice. However, the underlying mechanisms require further investigation. We further explored the potential beneficial effects of DAM-like cells in TBI model mice.

After TBI, microglia produce inflammatory cytokines to recruit additional immune cells and clear debris through phagocytosis [59], and the phagocytic roles of microglia are beneficial for tissue repair after injury [60]. However, previous studies revealed that the roles of TREM2 exhibits a dual nature. In a cuprizone-induced demyelination model, TREM2 facilitates microglial activation, enhances phagocytic capacity, and promotes the secretion of sufficient pro-inflammatory factors [61]. In a TBI model, TREM2 also recruits peripheral macrophages to the brain [62]. These results suggest that TREM2 is beneficial for microglia/macrophage activation and damaged cell debris clearance. However, prolonged activation of microglia in the later stages of TBI may result in persistent inflammation, leading to continuous neuronal loss and ultimately increasing the incidence of various neurodegenerative diseases [2]. Moreover, previous experiments have suggested that DAM may have special functions, such as enhanced phagocytic and surveillance capabilities [63]. The DAM-like cells in our TBI model also exhibited strong phagocytic abilities, assisting in the clearance of neuron debris, which removes necrotic cells, limits the extent of inflammation, and provides a favourable environment for repair. Additionally, VEGFa is an effective vascular remodelling factor that promotes angiogenesis [64]. Angiogenesis and vascular reconstruction in the perilesional zone can start as early as 3 dpi, often serving as favourable indicators associated with blood flow recovery [65]. Researchers have observed IBA1$^+$ VEGFa$^+$ branched microglia around the infarcted area in human stroke brain tissue [66]. Our study also revealed VEGFa$^+$ DAM-like cells in TBI model mice, indicating that DAM may promote vascular repair after TBI through the secretion of VEGFa. In animal stroke models, the administration of BDNF can protect neurons from apoptosis and reduce the infarct volume [67]. These findings suggest that increased levels of BDNF are beneficial for recovery after stroke. Elevated levels of BDNF after ischaemia have been reported to originate primarily from microglia [68]. BDNF has been shown to play a critical role in recovery processes following brain injury, such as neuronal survival, axonal sprouting, and synaptic formation [69]. Our study also revealed BDNF expression in DAM-like cells in TBI model mice, suggesting that DAM-like cells may improve TBI prognosis by secreting BDNF.

An increasing number of studies on immunometabolism have revealed the importance of metabolic reprogramming as a driving force for immune cell differentiation [70]. These studies highlight the unique role of metabolic reprogramming in driving immune cell differentiation. The immunometabolism status of DAM-like cells in the acute phase of TBI in mice remains unknown, suggesting that DAM-like cells in TBI model mice also require abundant energy to support their motility, proliferation, phagocytosis, and secretion. While TREM2 has been shown to induce glycolytic dysfunction in microglia in some chronic neurodegenerative diseases, its impact on microglial glycolysis in the acute phase of TBI is also still unknown. Additionally, further research is needed to investigate the interplay between glycolysis and the phenotypic transformation of DAM-like cells following TBI. Microglia are the major immune cells in the brain and exhibit different metabolic states in response to various external stimuli [46, 71, 72]. Resting microglia rely primarily on OXPHOS for ATP production, whereas inflammation-activated microglia depend on glycolysis [73]. The metabolic status of DAM-like cells remains poorly understood, and the metabolic state of DAM-like cells in a mouse TBI model has not been reported. To gain a better understanding of the true metabolic state of DAM-like cells, meanwhile no method yet for the in vitro induction of DAM using primary microglia, we directly obtained DAM-like cells from TBI model mice

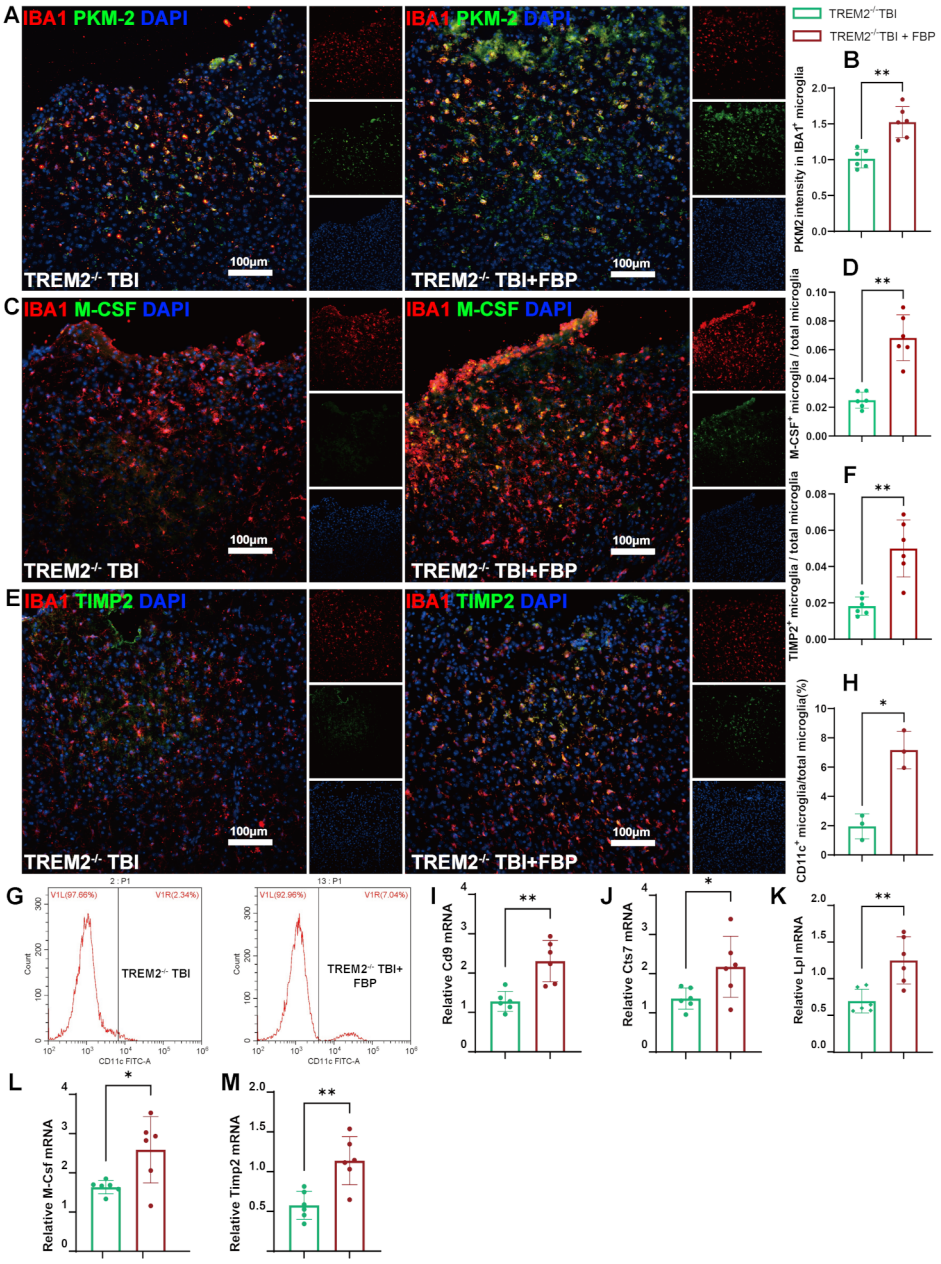

Fig. 8 A glycolysis enhancer, FBP, partially restored the impaired DAM-like phenotype in TREM2$^{-/-}$ TBI mice. **A** Representative images of immunofluorescence staining for PKM2 (green) in microglia (IBA1, red) of TREM2$^{-/-}$ TBI mice at 3 dpi, treated with or without FBP. Scale bar = 100 μm. **B** Quantitative analysis of PKM2 MFI in the microglia of TREM2$^{-/-}$ TBI mice at 3 dpi, treated with or without FBP. The data are expressed as the mean ± S.D. $^{**}P < 0.01$. $n = 6$ per group. **C**, **E** Representative images of immunofluorescence staining for M-CSF (**C**) or TIMP2 (**E**) and IBA1 in the cortex of TREM2$^{-/-}$ TBI mice at 3 dpi, treated with or without FBP. Scale bar = 100 μm. **D**, **F** Quantitative analysis of M-CSF^{+} (**D**) or TIMP^{+} (**F**) microglia to total microglia. The data are expressed as the mean ± S.D. $^{**}P < 0.01$. $n = 6$ mice per group. **G** Representative images of flow cytometric analysis depicting the proportion of CD11c^{+} (a DAM marker) cells within microglia (CD11b^{+}) sorted from TREM2$^{-/-}$ TBI mice at 3dpi, treated with or without FBP. **H** Quantitative analysis of CD11c^{+} cells to total microglia (CD11b^{+}) sorted from TREM2$^{-/-}$ TBI mice at 3dpi, treated with or without FBP. Data are represented as the mean ± S.D. $^{*}P < 0.05$. $n = 3$ mice per group. **I-M** The relative mRNA expression of Cd9 (**I**), Cst7 (**J**), Lpl (**K**), M-Csf (**L**), and Timp2 (**M**) in microglia sorted from TREM2$^{-/-}$ TBI mice at 3 dpi, treated with or without FBP. Data are presented as the mean ± S.D. $^{*}p < 0.05$, $^{**}p < 0.01$. $n = 6$ samples per group, each sample pooled from 3 mice brains

via single-cell dissociation techniques combined with magnetic bead separation. Although the sorting process may slightly interfere with the cellular state, this is currently the method that best preserves the original state of DAM-like cells in vivo while reducing interference from other cell types in the detection results. DAM-like cells isolated from model mice 3 dpi exhibited significantly increased glycolysis. Furthermore, our in vivo

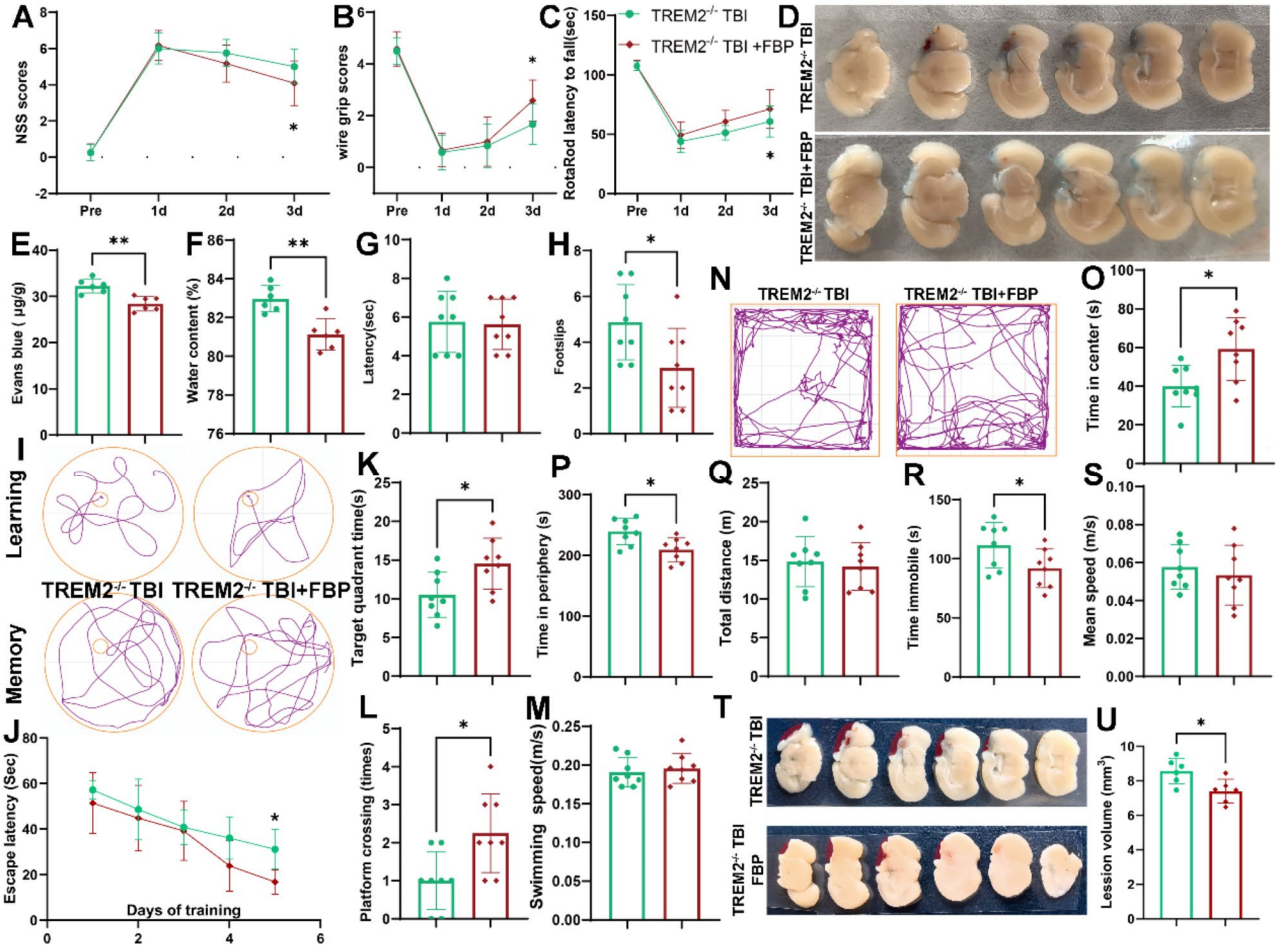

Fig. 9 FBP improved neurological recovery of TREM2$^{-/-}$ TBI mice. **A–C** Quantitative analysis of short-term neurological function by NSS scores (**A**), wire grip scores (**B**), and rotarod test (**C**). *$p < 0.05$ vs. TREM2$^{-/-}$ TBI + Vehicle, $n = 12$ mice per group. **D** Representative images of continuous coronal sections with Evans blue dye leakage for each group at 3 dpi. **E** Quantitative analysis of Evans blue leakage. The data are expressed as the means ± S.D. **$P < 0.01$. $n = 6$ mice per group. **F** Water content in brain tissue of each group at 3 dpi. The data are expressed as the means ± S.D. **$P < 0.01$. $n = 6$ mice per group. **G**, **H** Quantitative analysis of motor function at 13 dpi by the beam walking test. The data are expressed as the means ± S.D. *$p < 0.05$, $n = 8$ mice per group. **I** Representative images of the swimming routes of mice in the Morris water maze. Up panel: Learning stage; down panel: Memory stage. **J** Latency to find the platform in the learning stage. The data are expressed as the means ± S.D. *$P < 0.05$. $n = 8$ mice per group. **K-M** Quantitative analysis of the time in the target quadrant (**K**), the number of times crossing the platform (**L**) and the average swimming speed (**M**) in the probe trial. The data are expressed as the means ± S.D. *$P < 0.05$. $n = 8$ mice per group. **N** Representative images of the moving routes of mice in the open field test. **O-S** Quantitative analysis of central time (**O**), periphery time (**P**), total distance (**Q**), time immobile (**R**), and mean speed (**S**) in the open field test. The data are expressed as the means ± S.D. *$P < 0.05$. $n = 8$ mice per group. **T** Representative images of injury size in TREM2$^{-/-}$ TBI + Vehicle and TREM2$^{-/-}$ TBI + FBP mice at 21 dpi. **U** Quantification of brain tissue loss. The data are expressed as the means ± S.D. *$P < 0.05$. $n = 6$ mice per group

experiments corroborated the results of the in vitro experiments, showing that DAM-like cells in mice presented higher levels of glycolysis than those in the control group did, which may facilitate their phagocytosis, migration, and cytokine secretion.

Previous studies have demonstrated that TREM2 activation induces the transformation of microglia from a homeostatic state to a disease-associated phenotype [7]. Several in vivo studies have shown that TREM2-deficient microglia fail to acquire a complete DAM phenotype [74, 75]. Moreover, integrated metabolomics and RNA-seq analysis of TREM2-deficient microglia confirmed impaired mTOR activation, inhibited energy metabolism pathways and biosynthetic pathways, and decreased ATP levels. Therefore, TREM2 can maintain cellular energy and biosynthetic metabolism through the mTOR signalling pathway [27]. Under different stimuli or pathological conditions, metabolic changes in microglia are closely related to their function. TREM2-activated microglia acquire the critical ability to respond to, control, and eliminate neuroinflammatory stimuli, including enhancing migration, phagocytosis, survival, proliferation, and energy metabolism [76, 77]. Our experiments also revealed that TREM2 knockout leads to a significant

reduction in glycolysis in microglia after TBI, resulting in the inability of microglia after TBI to undergo glycolytic adaptation, which may lead to microglia being maintained in a homeostatic state and unable to transition into a DAM-like state. Similarly, inhibition of glycolysis resulted in a reduction in the proportion of DAM-like cells in TBI model mice, indicating the inhibition of the transformation of microglia into DAM-like cells. Furthermore, when glycolysis was increased in TREM2$^{-/-}$ TBI model mice via the use of glycolysis enhancers, the transformation of microglia into DAM-like cells was partially restored. In fact, studies have shown that the role of TREM2 is highly complex. In a TBI mouse model, TREM2 can regulate microglial lipid metabolism through the DHCR24/LXR pathway, thereby alleviating white matter injury and ultimately improving neurological outcomes [78]. Therefore, under TREM2 knockout conditions, promoting microglial glycolytic capacity through FBP may be partially effective in restoring their full functionality. Previous studies have shown that FBP can penetrate the cell membrane to affect intracellular processes related to glucose metabolism, and it can also exert effects extracellularly by modulating certain signals [79]. In the central nervous system, FBP may have a neuroprotective role in neurotoxicity and ischemic injury by influencing ATP levels (glycolysis), glutamate release, and oxidative stress [80]. However, the exact mechanisms remain unclear. Therefore, the effect of FBP on DAM glycolysis after TBI require more exploration.

Some previous studies have explored similar methods of regulating immune cell function and inducing phenotypic polarization by manipulating glucose or glycolytic metabolism. For example, induction of glycolysis in microglia can polarize them towards a mixed M1/M2 phenotype, while inhibiting glycolysis may impair their polarization to a proangiogenic phenotype [81]. Therefore, controlling the quantity and timing of DAM transformation through the regulation of glycolysis could potentially be a new strategy for TBI treatment.

This study has several limitations that should be acknowledged. First, we acknowledge the limitation of using single markers to identify DAM cells. Specifically, in our study, we used a combination of two markers (M-CSF and TIMP2) by immunofluorescence to detect the presence of DAM cells in the acute phase after TBI. Additionally, we performed microglia sorting followed by RT-qPCR analysis to quantify the changes in DAM cell marker expression. However, we recognize that more advanced approaches, such as single-cell sequencing and multi-omics, would be necessary to achieve a more comprehensive and accurate identification of DAM cells [82]. In the future, we will study DAM cells in TBI with multidimensional ways by integration of epigenetic, transcriptomic, metabolomics and proteomic data. Second, we were unable to directly perform Western blot analysis on sorted enriched microglia and DAM-like cells due to the minimal number of microglial specimens. Thus, it is possible that some other cells, such as neurons or astrocytes, may also contribute to the changes observed in the AKT/mTOR/HIF1α pathway following TBI. However, given that TREM2 is primarily expressed in microglia [23], we believe that the observed changes are mainly driven by microglia. Third, in vitro, there is currently no well-established protocol to induce DAM using primary microglia or BV2 cells. As such, our study, which modulates of glycolysis with 2-DG and FBP to induce phenotypic polarization of DAM-like cells in TBI mice, has not been fully validated by in vitro experiments and cannot exclude the potential interference from other cell types. However, the results, at least in part, conformed the role of the metabolic reprogramming in mediating DAM-like cell polarization in TBI mice. Finally, we used 2-DG and FBP to regulate glycolysis and examine the impact of metabolic reprogramming on the polarization of DAM-like cells in TBI mice. However, other potential functions of 2-DG, such as competitive inhibition of glucose transport, induction of apoptosis or autophagy, and its potential neuroprotective effects, should also be considered [83]. In addition, 2-DG administration might be related to the feeding rhythm of the mice [84], and this influence should be further explored in the future. Similarly, FBP not only supports glucose metabolism in the brain but also modulates reactive oxygen species production [85], exerts anti-inflammatory actions, and prevents intracellular K^+ depletion [86]. These multifaceted roles of 2-DG and FBP warrant further investigation in the context of TBI.

Taken together, these findings demonstrated that DAM-like cells were present in the acute phase of TBI and TREM2 might influence DAM-like cell transformation by modulating the glycolysis of microglia. Our results provide a new possible pathway for intervening TBI.

Supplementary Information

The online version contains supplementary material available at https://doi.org/10.1186/s12974-025-03337-2.

Supplementary Material 1

Acknowledgements

We would like to acknowledge the service provided by the Chongqing Key Laboratory of Neurology.

Author contributions

LW, JY, XCS, YZ and LL conceived and designed the study. LW, DQ OY, JY, YZ, ZSZ, YWW, YCC, ZL, and ST performed the experiments and analyzed the results. LW and JY wrote the manuscript. JY, XCS, and HT revised the manuscript. JY, YWW, ZSZ, HT and NNG participated in the data acquisition, analysis, and interpretation. XCS provided funding support. All authors read and approved the final manuscript.

Funding
This work was supported by the National Natural Science Foundation of China (NO. 82071397).

Data availability
No datasets were generated or analysed during the current study.

Declarations

Ethics approval and consent to participate
All experimental procedures used in this study were approved by the Animal Ethics Committee of the Chongqing Medical University.

Consent for publication
Not applicable.

Competing interests
The authors declare that they have no competing interests.

Author details
[1]Department of Neurosurgery, The First Affiliated Hospital of Chongqing Medical University, Chongqing 400016, China
[2]Department of Neurosurgery, The Second Clinical Medical College of North Sichuan Medical College, Beijing Anzhen Nanchong Hospital of Capital Medical University & Nanchong Central Hospital, Nanchong 637000, China
[3]Emergency Department, Chengdu First People's Hospital, Chengdu 610000, China
[4]Department of Neurosurgery, Suining Central Hospital, Suining 629000, China

Received: 10 October 2024 / Accepted: 6 January 2025
Published online: 13 January 2025

References

1. Kline AE, Leary JB, Radabaugh HL, Cheng JP, Bondi CO. Combination therapies for neurobehavioral and cognitive recovery after experimental traumatic brain injury: is more better? Prog Neurobiol. 2016;142:45–67.
2. Morganti-Kossmann MC, Semple BD, Hellewell SC, Bye N, Ziebell JM. The complexity of neuroinflammation consequent to traumatic brain injury: from research evidence to potential treatments. Acta Neuropathol. 2019;137:731–55.
3. Karve IP, Taylor JM, Crack PJ. The contribution of astrocytes and microglia to traumatic brain injury. Br J Pharmacol. 2016;173:692–702.
4. Olah M, Menon V, Habib N, Taga MF, Ma Y, Yung CJ, Cimpean M, Khairallah A, Coronas-Samano G, Sankowski R, et al. Single cell RNA sequencing of human microglia uncovers a subset associated with Alzheimer's disease. Nat Commun. 2020;11:6129.
5. Keren-Shaul H, Spinrad A, Weiner A, Matcovitch-Natan O, Dvir-Szternfeld R, Ulland TK, David E, Baruch K, Lara-Astaiso D, Toth B, et al. A Unique Microglia Type Associated with Restricting Development of Alzheimer's Disease. Cell. 2017;169:1276–e12901217.
6. Ennerfelt H, Frost EL, Shapiro DA, Holliday C, Zengeler KE, Voithofer G, Bolte AC, Lammert CR, Kulas JA, Ulland TK, Lukens JR. SYK coordinates neuroprotective microglial responses in neurodegenerative disease. Cell. 2022;185:4135–e41524122.
7. Krasemann S, Madore C, Cialic R, Baufeld C, Calcagno N, El Fatimy R, Beckers L, O'Loughlin E, Xu Y, Fanek Z, et al. The TREM2-APOE pathway drives the Transcriptional phenotype of dysfunctional microglia in neurodegenerative diseases. Immunity. 2017;47:566–e581569.
8. Mrdjen D, Pavlovic A, Hartmann FJ, Schreiner B, Utz SG, Leung BP, Lelios I, Heppner FL, Kipnis J, Merkler D, et al. High-dimensional single-cell mapping of Central Nervous System Immune cells reveals distinct myeloid subsets in Health, Aging, and Disease. Immunity. 2018;48:380–e395386.
9. Kim S, Lee W, Jo H, Sonn SK, Jeong SJ, Seo S, Suh J, Jin J, Kweon HY, Kim TK, et al. The antioxidant enzyme Peroxiredoxin-1 controls stroke-associated microglia against acute ischemic stroke. Redox Biol. 2022;54:102347.
10. Lu Y, Saibro-Girardi C, Fitz NF, McGuire MR, Ostach MA, Mamun-Or-Rashid ANM, Lefterov I, Koldamova R. Multi-transcriptomics reveals brain cellular responses to peripheral infection in Alzheimer's disease model mice. Cell Rep. 2023;42:112785.
11. Hakim R, Zachariadis V, Sankavaram SR, Han J, Harris RA, Brundin L, Enge M, Svensson M. Spinal cord Injury induces permanent reprogramming of Microglia into a Disease-Associated State which contributes to functional recovery. J Neurosci. 2021;41:8441–59.
12. Ritzel RM, Li Y, Lei Z, Carter J, He J, Choi HMC, Khan N, Li H, Allen S, Lipinski MM, et al. Functional and transcriptional profiling of microglial activation during the chronic phase of TBI identifies an age-related driver of poor outcome in old mice. Geroscience. 2022;44:1407–40.
13. Witcher KG, Bray CE, Chunchai T, Zhao F, O'Neil SM, Gordillo AJ, Campbell WA, McKim DB, Liu X, Dziabis JE, et al. Traumatic brain Injury causes chronic cortical inflammation and neuronal dysfunction mediated by Microglia. J Neurosci. 2021;41:1597–616.
14. Ferreira BL, Sousa MB, Leite GGF, Brunialti MKC, Nishiduka ES, Tashima AK, van der Poll T, Salomão R. Glucose metabolism is upregulated in the mononuclear cell proteome during sepsis and supports endotoxin-tolerant cell function. Front Immunol. 2022;13:1051514.
15. Hirschberger S, Strauß G, Effinger D, Marstaller X, Ferstl A, Müller MB, Wu T, Hübner M, Rahmel T, Mascolo H, et al. Very-low-carbohydrate diet enhances human T-cell immunity through immunometabolic reprogramming. EMBO Mol Med. 2021;13:e14323.
16. Guillot-Sestier MV, Araiz AR, Mela V, Gaban AS, O'Neill E, Joshi L, Chouchani ET, Mills EL, Lynch MA. Microglial metabolism is a pivotal factor in sexual dimorphism in Alzheimer's disease. Commun Biol. 2021;4:711.
17. Zanotelli MR, Zhang J, Reinhart-King CA. Mechanoresponsive metabolism in cancer cell migration and metastasis. Cell Metab. 2021;33:1307–21.
18. Vander Heiden MG, Cantley LC, Thompson CB. Understanding the Warburg effect: the metabolic requirements of cell proliferation. Science. 2009;324:1029–33.
19. O'Brien KL, Finlay DK. Immunometabolism and natural killer cell responses. Nat Rev Immunol. 2019;19:282–90.
20. Takeda H, Yamaguchi T, Yano H, Tanaka J. Microglial metabolic disturbances and neuroinflammation in cerebral infarction. J Pharmacol Sci. 2021;145:130–9.
21. Hu Y, Cao K, Wang F, Wu W, Mai W, Qiu L, Luo Y, Ge WP, Sun B, Shi L, et al. Dual roles of hexokinase 2 in shaping microglial function by gating glycolytic flux and mitochondrial activity. Nat Metab. 2022;4:1756–74.
22. Li Q, Barres BA. Microglia and macrophages in brain homeostasis and disease. Nat Rev Immunol. 2018;18:225–42.
23. Ulland TK, Colonna M. TREM2 - a key player in microglial biology and Alzheimer disease. Nat Rev Neurol. 2018;14:667–75.
24. Yan J, Zhang Y, Wang L, Li Z, Tang S, Wang Y, Gu N, Sun X, Li L. TREM2 activation alleviates neural damage via Akt/CREB/BDNF signalling after traumatic brain injury in mice. J Neuroinflammation. 2022;19:289.
25. Zhou Y, Song WM, Andhey PS, Swain A, Levy T, Miller KR, Poliani PL, Cominelli M, Grover S, Gilfillan S, et al. Human and mouse single-nucleus transcriptomics reveal TREM2-dependent and TREM2-independent cellular responses in Alzheimer's disease. Nat Med. 2020;26:131–42.
26. Piers TM, Cosker K, Mallach A, Johnson GT, Guerreiro R, Hardy J, Pocock JM. A locked immunometabolic switch underlies TREM2 R47H loss of function in human iPSC-derived microglia. Faseb j. 2020;34:2436–50.
27. Ulland TK, Song WM, Huang SC, Ulrich JD, Sergushichev A, Beatty WL, Loboda AA, Zhou Y, Cairns NJ, Kambal A, et al. TREM2 maintains microglial metabolic fitness in Alzheimer's Disease. Cell. 2017;170:649–e663613.
28. Saxton RA, Sabatini DM. mTOR Signaling in Growth, Metabolism, and Disease. Cell. 2017;168:960–76.
29. Schaible EV, Windschügl J, Bobkiewicz W, Kaburov Y, Dangel L, Krämer T, Huang C, Sebastiani A, Luh C, Werner C, et al. 2-Methoxyestradiol confers neuroprotection and inhibits a maladaptive HIF-1α response after traumatic brain injury in mice. J Neurochem. 2014;129:940–54.
30. Luo G, Wang X, Cui Y, Cao Y, Zhao Z, Zhang J. Metabolic reprogramming mediates hippocampal microglial M1 polarization in response to surgical trauma causing perioperative neurocognitive disorders. J Neuroinflammation. 2021;18:267.
31. Zhou WJ, Yang HL, Mei J, Chang KK, Lu H, Lai ZZ, Shi JW, Wang XH, Wu K, Zhang T, et al. Fructose-1,6-bisphosphate prevents pregnancy loss by inducing decidual COX-2(+) macrophage differentiation. Sci Adv. 2022;8:eabj2488.
32. Kim YC, Park TY, Baik E, Lee SH. Fructose-1,6-bisphosphate attenuates induction of nitric oxide synthase in microglia stimulated with lipopolysaccharide. Life Sci. 2012;90:365–72.

33. Cermak S, Meng Q, Peng K, Baldwin S, Mejías-Aponte CA, Yang Y, Lu H. Focal transcranial magnetic stimulation in awake rats: enhanced glucose uptake in deep cortical layers. J Neurosci Methods. 2020;339:108709.
34. Zhou C, Chen H, Zheng JF, Guo ZD, Huang ZJ, Wu Y, Zhong JJ, Sun XC, Cheng CJ. Pentraxin 3 contributes to neurogenesis after traumatic brain injury in mice. Neural Regen Res. 2020;15:2318–26.
35. Zhang Y, Wang L, Pan Q, Yang X, Cao Y, Yan J, Wang Y, Tao Y, Fan R, Sun X, Li L. Selective sphingosine-1-phosphate receptor 1 modulator attenuates blood-brain barrier disruption following traumatic brain injury by inhibiting vesicular transcytosis. Fluids Barriers CNS. 2022;19:57.
36. Wu Y, Pang J, Peng J, Cao F, Guo Z, Jiang L, Teng Z, Huang Z, Cheng C, Jiang Y, Sun X. Apolipoprotein E Deficiency Aggravates Neuronal Injury by Enhancing Neuroinflammation via the JNK/c-Jun Pathway in the Early Phase of Experimental Subarachnoid Hemorrhage in Mice. *Oxid Med Cell Longev* 2019, 2019:3832648.
37. Gu N, Yan J, Tang W, Zhang Z, Wang L, Li Z, Wang Y, Zhu Y, Tang S, Zhong J, et al. Prevotella copri transplantation promotes neurorehabilitation in a mouse model of traumatic brain injury. J Neuroinflammation. 2024;21:147.
38. Abdullah A, Zhang M, Frugier T, Bedoui S, Taylor JM, Crack PJ. STING-mediated type-I interferons contribute to the neuroinflammatory process and detrimental effects following traumatic brain injury. J Neuroinflammation. 2018;15:323.
39. Zhang X, Huang X, Hang D, Jin J, Li S, Zhu Y, Liu H. Targeting pyroptosis with nanoparticles to alleviate neuroinflammatory for preventing secondary damage following traumatic brain injury. Sci Adv. 2024;10:eadj4260.
40. Singh N, Benoit MR, Zhou J, Das B, Davila-Velderrain J, Kellis M, Tsai LH, Hu X, Yan R. BACE-1 inhibition facilitates the transition from homeostatic microglia to DAM-1. Sci Adv. 2022;8:eabo1286.
41. Broussard JI, Acion L, De Jesús-Cortés H, Yin T, Britt JK, Salas R, Costa-Mattioli M, Robertson C, Pieper AA, Arciniegas DB, Jorge R. Repeated mild traumatic brain injury produces neuroinflammation, anxiety-like behaviour and impaired spatial memory in mice. Brain Inj. 2018;32:113–22.
42. Parkhurst CN, Yang G, Ninan I, Savas JN, Yates JR 3rd, Lafaille JJ, Hempstead BL, Littman DR, Gan WB. Microglia promote learning-dependent synapse formation through brain-derived neurotrophic factor. Cell. 2013;155:1596–609.
43. Sierra A, Abiega O, Shahraz A, Neumann H. Janus-faced microglia: beneficial and detrimental consequences of microglial phagocytosis. Front Cell Neurosci. 2013;7:6.
44. Mastorakos P, Mihelson N, Luby M, Burks SR, Johnson K, Hsia AW, Witko J, Frank JA, Latour L, McGavern DB. Temporally distinct myeloid cell responses mediate damage and repair after cerebrovascular injury. Nat Neurosci. 2021;24:245–58.
45. Xiong Y, Zhang Y, Mahmood A, Meng Y, Qu C, Chopp M. Erythropoietin mediates neurobehavioral recovery and neurovascular remodeling following traumatic brain injury in rats by increasing expression of vascular endothelial growth factor. Transl Stroke Res. 2011;2:619–32.
46. Baik SH, Kang S, Lee W, Choi H, Chung S, Kim JI, Mook-Jung I. A breakdown in metabolic reprogramming causes Microglia Dysfunction in Alzheimer's Disease. Cell Metab. 2019;30:493–e507496.
47. Ajami B, Bennett JL, Krieger C, Tetzlaff W, Rossi FM. Local self-renewal can sustain CNS microglia maintenance and function throughout adult life. Nat Neurosci. 2007;10:1538–43.
48. Colton C, Wilcock DM. Assessing activation states in microglia. CNS Neurol Disord Drug Targets. 2010;9:174–91.
49. Guo Y, Dai W, Zheng Y, Qiao W, Chen W, Peng L, Zhou H, Zhao T, Liu H, Zheng F, Sun P. Mechanism and regulation of Microglia polarization in Intracerebral Hemorrhage. Molecules 2022, 27.
50. Schwabenland M, Brück W, Priller J, Stadelmann C, Lassmann H, Prinz M. Analyzing microglial phenotypes across neuropathologies: a practical guide. Acta Neuropathol. 2021;142:923–36.
51. Xu YJ, Au NPB, Ma CHE. Functional and phenotypic diversity of Microglia: implication for Microglia-based therapies for Alzheimer's Disease. Front Aging Neurosci. 2022;14:896852.
52. Tay TL, Sagar, Dautzenberg J, Grün D, Prinz M. Unique microglia recovery population revealed by single-cell RNAseq following neurodegeneration. Acta Neuropathol Commun. 2018;6:87.
53. Sousa C, Golebiewska A, Poovathingal SK, Kaoma T, Pires-Afonso Y, Martina S, Coowar D, Azuaje F, Skupin A, Balling R et al. Single-cell transcriptomics reveals distinct inflammation-induced microglia signatures. EMBO Rep 2018, 19.
54. Masuda T, Sankowski R, Staszewski O, Böttcher C, Amann L, Sagar, Scheiwe C, Nessler S, Kunz P, van Loo G, et al. Spatial and temporal heterogeneity of mouse and human microglia at single-cell resolution. Nature. 2019;566:388–92.
55. Almeida-Suhett CP, Li Z, Marini AM, Braga MF, Eiden LE. Temporal course of changes in gene expression suggests a cytokine-related mechanism for long-term hippocampal alteration after controlled cortical impact. J Neurotrauma. 2014;31:683–90.
56. Götzl JK, Brendel M, Werner G, Parhizkar S, Sebastian Monasor L, Kleinberger G, Colombo AV, Deussing M, Wagner M, Winkelmann J et al. Opposite microglial activation stages upon loss of PGRN or TREM2 result in reduced cerebral glucose metabolism. EMBO Mol Med 2019, 11.
57. Mazaheri F, Snaidero N, Kleinberger G, Madore C, Daria A, Werner G, Krasemann S, Capell A, Trümbach D, Wurst W, et al. TREM2 deficiency impairs chemotaxis and microglial responses to neuronal injury. EMBO Rep. 2017;18:1186–98.
58. Park G, Suh JH, Han SJ. Transcranial direct current stimulation for balance and gait in repetitive mild traumatic brain injury in rats. BMC Neurosci. 2021;22:26.
59. Bachiller S, Jiménez-Ferrer I, Paulus A, Yang Y, Swanberg M, Deierborg T, Boza-Serrano A. Microglia in Neurological diseases: a Road Map to Brain-Disease Dependent-Inflammatory response. Front Cell Neurosci. 2018;12:488.
60. Doust YV, Bindoff A, Holloway OG, Wilson R, King AE, Ziebell JM. Temporal changes in the microglial proteome of male and female mice after a diffuse brain injury using label-free quantitative proteomics. Glia. 2023;71:880–903.
61. Cantoni C, Bollman B, Licastro D, Xie M, Mikesell R, Schmidt R, Yuede CM, Galimberti D, Olivecrona G, Klein RS, et al. TREM2 regulates microglial cell activation in response to demyelination in vivo. Acta Neuropathol. 2015;129:429–47.
62. Saber M, Kokiko-Cochran O, Puntambekar SS, Lathia JD, Lamb BT. Triggering receptor expressed on myeloid cells 2 Deficiency alters Acute Macrophage distribution and improves recovery after traumatic brain Injury. J Neurotrauma. 2017;34:423–35.
63. Deczkowska A, Keren-Shaul H, Weiner A, Colonna M, Schwartz M, Amit I. Disease-Associated Microglia: a Universal Immune Sensor of Neurodegeneration. Cell. 2018;173:1073–81.
64. Reitmeir R, Kilic E, Reinboth BS, Guo Z, ElAli A, Zechariah A, Kilic U, Hermann DM. Vascular endothelial growth factor induces contralesional corticobulbar plasticity and functional neurological recovery in the ischemic brain. Acta Neuropathol. 2012;123:273–84.
65. Hayashi T, Noshita N, Sugawara T, Chan PH. Temporal profile of angiogenesis and expression of related genes in the brain after ischemia. J Cereb Blood Flow Metab. 2003;23:166–80.
66. Choi BR, Johnson KR, Maric D, McGavern DB. Monocyte-derived IL-6 programs microglia to rebuild damaged brain vasculature. Nat Immunol. 2023;24:1110–23.
67. Jang SW, Liu X, Yepes M, Shepherd KR, Miller GW, Liu Y, Wilson WD, Xiao G, Blanchi B, Sun YE, Ye K. A selective TrkB agonist with potent neurotrophic activities by 7,8-dihydroxyflavone. Proc Natl Acad Sci U S A. 2010;107:2687–92.
68. Cramer T, Gill R, Thirouin ZS, Vaas M, Sampath S, Martineau F, Noya SB, Panzanelli P, Sudharshan TJJ, Colameo D, et al. Cross-talk between GABAergic postsynapse and microglia regulate synapse loss after brain ischemia. Sci Adv. 2022;8:eabj0112.
69. Huang EJ, Reichardt LF. Neurotrophins: roles in neuronal development and function. Annu Rev Neurosci. 2001;24:677–736.
70. Zhu M, Wang X, Schultzberg M, Hjorth E. Differential regulation of resolution in inflammation induced by amyloid-β42 and lipopolysaccharides in human microglia. J Alzheimers Dis. 2015;43:1237–50.
71. Hu Y, Mai W, Chen L, Cao K, Zhang B, Zhang Z, Liu Y, Lou H, Duan S, Gao Z. mTOR-mediated metabolic reprogramming shapes distinct microglia functions in response to lipopolysaccharide and ATP. Glia. 2020;68:1031–45.
72. Orihuela R, McPherson CA, Harry GJ. Microglial M1/M2 polarization and metabolic states. Br J Pharmacol. 2016;173:649–65.
73. Cheng J, Zhang R, Xu Z, Ke Y, Sun R, Yang H, Zhang X, Zhen X, Zheng LT. Early glycolytic reprogramming controls microglial inflammatory activation. J Neuroinflammation. 2021;18:129.
74. Lee CYD, Daggett A, Gu X, Jiang LL, Langfelder P, Li X, Wang N, Zhao Y, Park CS, Cooper Y, et al. Elevated TREM2 gene dosage reprograms Microglia Responsivity and ameliorates pathological phenotypes in Alzheimer's Disease models. Neuron. 2018;97:1032–e10481035.
75. Nugent AA, Lin K, van Lengerich B, Lianoglou S, Przybyla L, Davis SS, Llapashtica C, Wang J, Kim DJ, Xia D, et al. TREM2 regulates microglial cholesterol metabolism upon chronic phagocytic challenge. Neuron. 2020;105:837–e854839.

76. Vilalta A, Zhou Y, Sevalle J, Griffin JK, Satoh K, Allendorf DH, De S, Puigdellívol M, Bruzas A, Burguillos MA, et al. Wild-type sTREM2 blocks Aβ aggregation and neurotoxicity, but the Alzheimer's R47H mutant increases Aβ aggregation. J Biol Chem. 2021;296:100631.
77. McQuade A, Kang YJ, Hasselmann J, Jairaman A, Sotelo A, Coburn M, Shabestari SK, Chadarevian JP, Fote G, Tu CH, et al. Gene expression and functional deficits underlie TREM2-knockout microglia responses in human models of Alzheimer's disease. Nat Commun. 2020;11:5370.
78. Li Z, Yu S, Li L, Zhou C, Wang L, Tang S, Gu N, Zhang Z, Huang Z, Chen H, et al. TREM2 alleviates white matter injury after traumatic brain injury in mice might be mediated by regulation of DHCR24/LXR pathway in microglia. Clin Transl Med. 2024;14:e1665.
79. Wheeler TJ, McCurdy JM, denDekker A, Chien S. Permeability of fructose-1,6-bisphosphate in liposomes and cardiac myocytes. Mol Cell Biochem. 2004;259:105–14.
80. Seok SM, Kim JM, Park TY, Baik EJ, Lee SH. Fructose-1,6-bisphosphate ameliorates lipopolysaccharide-induced dysfunction of blood-brain barrier. Arch Pharm Res. 2013;36:1149–59.
81. Liu Z, Xu J, Ma Q, Zhang X, Yang Q, Wang L, Cao Y, Xu Z, Tawfik A, Sun Y et al. Glycolysis links reciprocal activation of myeloid cells and endothelial cells in the retinal angiogenic niche. Sci Transl Med 2020, 12.
82. Paolicelli RC, Sierra A, Stevens B, Tremblay ME, Aguzzi A, Ajami B, Amit I, Audinat E, Bechmann I, Bennett M, et al. Microglia states and nomenclature: a field at its crossroads. Neuron. 2022;110:3458–83.
83. Pajak B, Siwiak E, Sołtyka M, Priebe A, Zieliński R, Fokt I, Ziemniak M, Jaśkiewicz A, Borowski R, Domoradzki T, Priebe W. 2-Deoxy-d-Glucose and its analogs: from Diagnostic to Therapeutic agents. Int J Mol Sci 2019, 21.
84. Wang Z, Ji S, Huang Y, Liao K, Cui Z, Chu F, Chen J, Tang S. The daily gene transcription cycle in mouse retina. Exp Eye Res. 2021;207:108565.
85. Catarina AV, Luft C, Greggio S, Venturin GT, Ferreira F, Marques EP, Rodrigues L, Wartchow K, Leite MC, Gonçalves CA, et al. Fructose-1,6-bisphosphate preserves glucose metabolism integrity and reduces reactive oxygen species in the brain during experimental sepsis. Brain Res. 2018;1698:54–61.
86. Alva N, Alva R, Carbonell T. Fructose 1,6-Bisphosphate: a Summary of its cytoprotective mechanism. Curr Med Chem. 2016;23:4396–417.

Publisher's note